

Title

Origin of anomalous p-type conductivity in monolayer Fe-doped MoS₂

Authors

Xiangning Quan^{1, †}, Xiaoqiu Yuan^{2, †}, Junwei Zhang^{1, †}, Xuebing Peng^{3, †}, Helin Mei^{3, †}, Cheng Yan⁴, Hong Zhang^{5,6}, Hongli Li⁷, Daqiang Gao³, Yongjian Wang¹, Mingsu Si¹, Lili Zhang^{1, *}, Anmin Zhang^{3, *}, Zongyuan Zhang^{2, *}, Lei Shan², and Yong Peng^{1, *}

Affiliations

¹School of Materials and Energy, or Electron Microscopy Centre of Lanzhou University, Lanzhou University, Lanzhou, China.

²Information Materials and Intelligent Sensing Laboratory of Anhui Province, Center of Free Electron Laser and High Magnetic Field, Institutes of Physical Science and Information Technology, Anhui University, Hefei, China.

³School of Physical Science and Technology, Lanzhou University, Lanzhou, China.

⁴School of Chemistry, Faculty of Science, The University of Sydney, Sydney, Australia.

⁵Yunnan Key Laboratory of Electromagnetic Materials and Devices, School of Materials and Energy, Yunnan University, Kunming, China.

⁶Electron Microscopy Center, Yunnan University, Kunming, China.

⁷State Key Laboratory of Solid Lubrication, Lanzhou Institute of Chemical Physics, Chinese Academy of Sciences, Lanzhou, China

*Corresponding author. Email: zll@lzu.edu.cn (L.Z.); amzhang@lzu.edu.cn (A.Z.); zongyuanzhang@ahu.edu.cn(Z.Z.); pengy@lzu.edu.cn (Y.P.)

†These authors contributed equally.

Abstract

Substitutional doping effectively modulates carrier polarity of semiconducting two-dimensional (2D) transition metal dichalcogenides (TMDs) like MoS₂. Although Fe doping typically induces n-type conductivity in monolayer MoS₂, anomalous p-type behavior has also been experimentally reported, the origin of which remains unresolved. Here, we prove that this anomalous p-type conductivity originates from defect associates formed through interactions between Fe dopants and S atoms, which consists of three Fe substituting Mo (Fe_{Mo}) point defects arranged into an equilateral triangle with a central S atom, denoted as 3Fe_{Mo}-S associate. Its p-type effect is directly verified through scanning tunneling microscopy/scanning tunneling spectroscopy (STM/STS) measurement, in sharp contrast to the n-type behavior induced by isolated Fe_{Mo} point defects, and the conclusion is further supported by electrical transport measurements and first-principles calculations. Similar 3Fe_W-S associates and their p-type doping effect are also identified in monolayer Fe-doped WS₂. This work resolves a longstanding controversy and highlights the critical role of defect associates in modulating properties of 2D TMDs.

Teaser

This work clarifies that the anomalous p-type conductivity induced by Fe doping in MoS₂ arises from the associates composed of Fe dopants and S atoms.

MAIN TEXT

Introduction

Semiconducting 2D TMDs, such as MoS₂ and WS₂, represent promising channel materials for post-Moore electronics due to their exceptional electrical properties arising from atomic thickness (1-4). Carrier polarity manipulation for 2D TMDs is significant and a prerequisite for construction of 2D p-n junctions to promote their real-world utilization. Defects play a critical, even decisive role in modulating 2D TMDs' electrical properties. So far, various types of point defects including vacancies (5, 6), substitutional dopants (7-9), antisite defects (10, 11), and interstitial atoms (12, 13) have been intensively investigated to regulate the carrier polarity of 2D TMDs, among which

substitution doping is believed to be one of the most important and effective strategies for its high controllability and stability.

Transition metals serve as promising dopants for 2D TMDs because of their ability to form stable covalent bonds with the host lattice. Generally speaking, when transition metals such as Re and Mn (*14, 15*) with more valence electrons than that of transition metal M in MX_2 (M=Mo, W, X=S, Se) substitute M atoms, system will be lead to n-type doping (electron doping), meanwhile for transition metals with less valence electrons like V, Nb, and Ta, p-type doping (hole doping) is achieved (*16-18*). However, as a typical transition metal, Fe doping in MoS_2 brings contradictory results, in which both enhanced n-type doping and p-type doping has been observed and reported by different groups (*19-23*). It is widely accepted that isolated Fe dopants can enhance the n-type conductivity of MoS_2 because Fe has two more valence electrons than Mo and they completely or partially release these electrons when substitute Mo atoms. However, the origin of anomalous p-type doping is still unclear.

In this study, we provide direct evidence that the anomalous p-type doping in monolayer Fe-doped MoS_2 arises from the Fe dopant-related defect associates, which formed through interactions between Fe atoms and S atoms. The atomic-resolution high angle annular dark field scanning transmission electron microscopy (HAADF-STEM) images confirm the real-space atomic structure of the single associate is three nearest-neighboring Fe_{Mo} point defects arranging into a triangular configuration with a S atom at the center, which is labelled as $3\text{Fe}_{\text{Mo}}\text{-S}$ associate here. Stark contrast to isolated Fe_{Mo} point defects that contribute electron doping to monolayer MoS_2 (*19-21*), the STM/STS measurements demonstrate that single $3\text{Fe}_{\text{Mo}}\text{-S}$ associate induces acceptor states above the valence band maximum (VBM) of MoS_2 , confirming its hole doping effect. This hole doping role is further verified by both electrical transport measurements and theoretical calculations. Similar $3\text{Fe}_{\text{W}}\text{-S}$ associates and their hole doping effect are also observed in monolayer Fe-doped WS_2 . This study reconciles a long-time inconsistency observed in Fe-doped MoS_2 and demonstrates the significance of defect associates in tailoring properties of 2D TMDs.

Results

Recognition of $3\text{Fe}_{\text{M}_0}\text{-S}$ associates in monolayer Fe-doped MoS_2

Fe-doped and pristine MoS_2 monolayers were synthesized by chemical vapor deposition (CVD) method using $\text{Fe}_2\text{Mo}_3\text{O}_{12}$ and MoO_3 as precursors respectively (Methods and fig. S1 for details). Fe-doped MoS_2 monolayers exhibit a triangular morphology as displayed in optical image (inset, Fig. 1A). The height of a freshly prepared monolayer Fe-doped MoS_2 flake is determined to be 0.96 nm as measured by atomic force microscope (fig. S2), confirming its monolayer feature. Figure 1A shows the Raman spectra of monolayer Fe-doped and pristine MoS_2 . Monolayer pristine MoS_2 shows two characteristic Raman peaks locating at 385.1 cm^{-1} and 404.5 cm^{-1} , corresponding to the E' and A_1' modes, respectively (24, 25). After incorporating Fe atoms into MoS_2 , two new peaks locating at 349.4 cm^{-1} and 375.8 cm^{-1} are observed, which come from zone-edge phonon modes induced by Fe doping-related disorders (Supplementary Text S1, fig. S3 and Table S1). Figure 1B shows the fine-scanning Fe 2p, Mo 3d, and S 2p X-ray photoelectron spectroscopy (XPS) spectra of Fe-doped (upper part) and pristine (lower part) MoS_2 . The observation of Fe $2p_{1/2}$ peak (720.8 eV), Fe $2p_{3/2}$ peak (707.0 eV) along with its satellite peak (711.4 eV) in Fe-doped MoS_2 unambiguously confirm the Fe incorporation in monolayer MoS_2 . Compared with XPS spectra of the pristine MoS_2 , the peak positions of both Mo and S in Fe-doped MoS_2 are shifted 0.8 eV toward lower binding energies. This indicates that the introduction of Fe weakens Mo-S bonds and implies a downshift of the Fermi level (E_F) toward the VBM, which is a characteristic of hole doping for monolayer MoS_2 (26). In addition, the photoluminescence spectra, XPS survey scan, and energy dispersive X-ray spectrum (EDX) of samples collectively validate the incorporation of Fe into MoS_2 (figs. S4 to S6).

To confirm the accurate position of Fe atoms in monolayer MoS_2 , we performed atomic-resolution imaging on the samples using spherical aberration-corrected scanning transmission electron microscopy (Cs-STEM). Figure 1C shows the enlarged atomic-resolution HAADF-STEM image of monolayer Fe-doped MoS_2 cut from the white dashed box area in another HAADF-STEM image (fig. S7D). Since the contrast

intensity in HAADF-STEM image is proportional to the atomic number $Z^{1.7}$ (27), the brightest atoms in Fig. 1C can be indexed to Mo atoms. Mo atoms and 2S columns form the hexagonal crystal structure of monolayer MoS₂ as indicated in the upper left of Fig. 1C. Due to the smaller atomic number of Fe than Mo, its contrast intensity is lower than Mo and some darker spots in the sublattice of Mo sites are observed as highlighted with white circles in Fig. 1C, which correspond to Fe atoms. In order to verify this further, a simulated HAADF-STEM image by QSTEM software (28) containing an isolated Fe_{Mo} point defect is presented in Fig. 1D. The experimental image, which is cut from the yellow rectangle in fig. S7D, corresponding to the simulated one is displayed in Fig. 1E. The intensity profile of five atoms along the yellow solid line in Fig. 1E (left to right: Mo-Mo-darker spot-Mo-Mo) closely matches with the red broken line in Fig. 1D (left to right: Mo-Mo-Fe-Mo-Mo) as displayed in Fig. 1F, confirming that the darker spot in Fig. 1E is Fe atom. This demonstrates that Fe atoms substitute Mo atoms and this substitution is achieved by a random way (fig. S7D). Besides isolated Fe_{Mo} point defects, three nearest-neighboring Fe atoms arrange into a triangle can be found as marked with a yellow triangle in Fig. 1C. It is noted that the brightness of the center of the triangle corresponding to the sublattice of S atoms is approximately half that of the other equivalent sites, which may be caused by the loss of a single S atom from the central S-column site. To confirm this, similarly, a simulated HAADF-STEM image containing one triangle configuration is presented in Fig. 1G. Its corresponding experimental image cutting from the blue rectangle in fig. S7D is shown in Fig. 1H. The contrast intensity curve of five atomic positions measured along the light blue solid line in Fig. 1H is highly consistent with the contrast intensity curve measured along the dark blue broken line in Fig. 1G (left to right: 2S-2S-S-2S-2S) as shown in Fig. 1I, unambiguously confirming that only one S atom left in the center of the triangle. Thus, the atomic structure of this defect associate is determined, which is composed of three nearest-neighboring Fe_{Mo} point defects and one S atom and is marked as 3Fe_{Mo}-S associate. Its corresponding top view and side view of atomic configurations are displayed in Fig. 1J. This schematic diagram of atomic structure shows the lattice distortion of monolayer MoS₂ caused by Fe dopants. It is noticed that the S and Fe

atoms in this structure tend to be coplanar due to the lowest system energy (Supplementary Text S2, fig. S10). Above analyses reveal that there are two defect types in monolayer Fe-doped MoS₂, one is isolated Fe_{M0} point defect and the other is 3Fe_{M0}-S associate.

More isolated Fe_{M0} point defects and 3Fe_{M0}-S associates in monolayer Fe-doped MoS₂ can be observed in fig. S7D, and the Fe doping concentration is calculated to be 6.9 at. % (Supplementary Text S3), in which Fe atoms forming 3Fe_{M0}-S associates account for approaching 40% of the total Fe atoms (fig. S8). Moreover, monolayer MoS₂ with tunable Fe doping concentration can be synthesized by replacing Fe₂Mo₃O₁₂ precursor with FeS₂ and MoO₃ and by tuning their atomic ratio (fig. S9). Further analyses confirm that with the increase of FeS₂ content, both the Fe doping concentration and the proportion of Fe atoms in 3Fe_{M0}-S associates gradually increase, providing possibility for the realization of defect concentration-dependent properties for MoS₂. In addition, the 3Fe_{M0}-S associates in individual nanosheets exhibit predominant unidirectional alignment (figs. S7E and S9) as the central S atom effectively lowers their formation energy (Supplementary Text S4, figs. S11 and S12).

Detection of the hole doping role of 3Fe_{M0}-S associates for monolayer MoS₂

After transferring monolayer Fe-doped MoS₂ flakes onto Au substrate and cleaning its surface by annealing under ultrahigh vacuum conditions at ~200 °C, we conducted the STM/STS characterizations in order to probe defect induced electronic states in the sample. Figure 2A shows the STM topography measured in the constant current mode. Stacking monolayer Fe-doped MoS₂ on an Au (111) substrate forms hexagonal moiré patterns as depicted in Fig. 2A, and the fast Fourier transform (FFT) in the inset confirms their six-fold symmetry. The observed moiré period is ~3.3 nm, which is consistent with previous studies on stacking monolayer MoS₂ on Au (111) (29, 30). The diagonal line in Fig. 2A comes from a substrate step on Au surface, which can be clearly seen in its corresponding 3D image (fig. S13A). Before STS measurements, identification of Fe_{M0} point defects and 3Fe_{M0}-S associates in STM topography image is essential. Firstly, the simulated STM images for single Fe dopant in monolayer MoS₂

in a previous research showed that a triangular bright spot would appear near an isolated Fe_{M_0} point defect in constant current mode, which comes from the local density of states of S atoms near the Fe atom (31). Based on this, the triangular bright spots in Fig. 2A can be indexed to Fe_{M_0} point defects, and three isolated Fe_{M_0} point defects in Fig. 2A marked with red circles are labelled as defect #1(1), defect #1(2) and defect #1(3), respectively. The distance between adjacent vertices of the bright triangle is ~ 1.2 nm (inset, Fig. 2C), which is twice as long as the distance between two adjacent vertices at the S vacancy (~ 0.7 nm) that has been observed (32), completely excluding the interference of S vacancies as the defect of this morphology. Secondly, sulfur vacancy-related defects typically appear as dark triangles in STM images (33, 34), coupling with the electronic state discussed later, we can identify the dark spot marked with defect #2(1) in Fig. 2A as a 3Fe_{M_0} -S associate.

The differential conductance (dI/dV) spectra measured on top region (orange point) and hollow region (purple point) on monolayer pristine MoS_2 are presented in Fig. 2B. A gap ranging from -1.25 V to 0.25 V in the spectra of density of states (DOS) can be seen, which is the bandgap of monolayer pristine MoS_2 stacking on Au (111). The measured bandgap of 1.5 eV is smaller than that of the free-standing monolayer MoS_2 (~ 1.7 eV) for the strong hybridization between the electronic states of MoS_2 and Au substrate (35). The peak labelled as Γ_1 located at ~ 0.9 V is interpreted as a hybrid Au- MoS_2 or an interface state. The other peak Γ_2 located at ~ 1.4 V corresponds to the prominent resonances at the Γ point in Brillouin zone, similar to the case in free-standing MoS_2 . In the valence band, the peak measured at top spot region is shifted to higher voltage than that at hollow spot, which can be explained by the unequal hybridization between these states near Q point in Brillouin zone with Au substrate (36). The dI/dV spectra collected along the arrowed line (left inset, Fig. 2C) approaching the center of defect #1(1) are displayed in Fig. 2C. At position corresponding to the end of the arrow, that is, away from the center of defect #1(1), a DOS peak at 0.95 V still can be observed. With the approaching of the center of defect #1(1), this peak becomes stronger and shifts to lower voltage, which can be due to the bandgap decrease accompanied by an electron doping effect induced by isolated Fe_{M_0} point defect (34).

The spectra of a $3\text{Fe}_{\text{Mo}}\text{-S}$ associate shown in Fig. 2D were also studied by the same way as that of Fe_{Mo} point defect. As the center of defect #2(1) is approached, a DOS peak above the VBM of monolayer MoS_2 gradually appears at -0.8 V. The appearance of this peak can be contributed to the acceptor states induced by defect #2(1), drawing the conclusion that $3\text{Fe}_{\text{Mo}}\text{-S}$ associates introduce holes into the system. We also noticed other evolutions in the electronic states near defect #2(1) such as the increase in DOS at valence band edge around -1.5 V, which may originate from the upward shift of the valence band or the influence of moiré patterns as described in Fig. 2A. More STS measurements on other isolated Fe_{Mo} point defects and $3\text{Fe}_{\text{Mo}}\text{-S}$ associates show similar results (fig. S13, B and C) with that in Fig. 2 (C and D). All above STS results demonstrate that the isolated Fe_{Mo} point defect and $3\text{Fe}_{\text{Mo}}\text{-S}$ associate indeed produces electron doping and hole doping for monolayer MoS_2 , respectively.

Electrical transport properties of Fe-doped and pristine MoS_2 monolayers

In order to verify above inference, the electrical transport properties of Fe-doped and pristine MoS_2 monolayers were measured. Figure 3A shows the schematic field-effect transistor (FET) device structure made of monolayer Fe-doped MoS_2 . Figure 3B presents the output characteristics of monolayer Fe-doped MoS_2 , along with an optical image of a representative device (inset). The Fe-doped monolayer exhibits highly linear output behavior, in contrast to the pronounced nonlinearity observed in pristine MoS_2 (fig. S14), indicating that Fe doping significantly improves the electrical contact between the semiconductor and the metal electrodes. Figure 3 (C and D) shows the transfer curves of monolayer pristine and Fe-doped MoS_2 , respectively. The pristine sample exhibits well n-type semiconductor behavior with an on/off ratio of $\sim 10^6$ at $V_{\text{ds}}=5.0$ V, while the Fe-doped sample shows degenerate p-type conductivity behavior. Contrary to the established view that Fe_{Mo} point defects act as electron donors in monolayer MoS_2 for more valence electrons (Fe: $[\text{Ar}]3\text{d}^64\text{s}^2$, Mo: $[\text{Kr}]4\text{d}^55\text{s}^1$), our Fe-doped samples exhibit degenerate p-type conductivity. We attribute this to the compensatory hole doping from $3\text{Fe}_{\text{Mo}}\text{-S}$ defect associates, which outweighs the electron donation from isolated Fe_{Mo} point defects. This interpretation is consistent with

above STS results.

Exploration on the origin of hole doping of 3Fe_{M0}-S associate

To understand the n-type and p-type conductivities induced by different defect configurations in monolayer Fe-doped MoS₂, we performed first-principles calculations of the electronic band structures of pristine monolayer MoS₂ as well as systems containing an isolated Fe_{M0} point defect or a 3Fe_{M0}-S associate. A 4×4×1 supercell of monolayer MoS₂ was chosen to mimic the desired defects (fig. S11, A and B). The pristine monolayer MoS₂ exhibits a direct bandgap of 1.71 eV (fig. S15), consistent with previous reports (37). Figure 4A shows the band structure of monolayer MoS₂ containing one isolated Fe_{M0} point defect, demonstrating that substituting one Mo atom with Fe introduces four flat defect bands within the band gap near the E_F . Our calculated results found that the metal-S bond length is reduced from 2.41 Å (Mo-S bond) in pristine MoS₂ to 2.28 Å (Fe-S bond) in the sample containing one isolated Fe_{M0} point defect (fig. S11A). The decreased bond length enhances the crystal field in the trigonal prismatic coordination of S ligands, leading to the splitting of the *d*-orbitals of the Fe atom. As shown in the projected density of states (PDOS) in Fig. 4B, the flat band just below the E_F is dominated by the Fe- d_{z^2} orbital, while the degenerate Fe- d_{xy} and Fe- $d_{x^2-y^2}$ orbitals mainly contribute to the flat band just above E_F . Two additional bands at ~0.75 eV above E_F originate from the Fe- d_{xz} and Fe- d_{yz} orbitals. The presence of unoccupied bands above the E_F suggests n-type doping in the monolayer MoS₂. By integrating PDOS around 0.75 eV, it is found that per Fe_{M0} point defect provides 1.49 electrons for monolayer MoS₂.

The band structure of monolayer MoS₂ with a 3Fe_{M0}-S associate is shown in Fig. 4C. Increased Fe substitution introduces additional in-gap bands, and the E_F intersecting these impurity bands indicates high electrical conductivity, consistent with the electrical transport results in Fig. 3D. Notably, the PDOS in Fig. 4D exhibits a sharp peak of ~195.0 states/eV near -0.58 eV above the VBM. This localized state can accommodate more electrons from valence band of monolayer MoS₂, which plays a crucial role to the hole doping. Theoretical calculations show that every 3Fe_{M0}-S

associate donates 11.14 holes to the system, exceeding the electron contribution from a single Fe_{Mo} point defect by approximately an order of magnitude. This also explains why even in the monolayer MoS_2 system where the concentration of $3\text{Fe}_{\text{Mo}}\text{-S}$ associates is much less than that of isolated Fe_{Mo} point defects, the sample still features a degenerate p-type semiconductor.

$3\text{Fe}_{\text{W}}\text{-S}$ associates in monolayer Fe-doped WS_2

In order to explore whether similar associates can exist stably in 2D semiconductors analogous to MoS_2 and how they affect the properties of these materials, monolayer Fe-doped WS_2 was synthesized (see Methods). The EDX spectrum of Fe-doped WS_2 flakes confirms the existence of Fe atoms in WS_2 (fig. S16). Figure 5A shows the atomic-resolution HAADF-STEM image of a monolayer Fe-doped WS_2 . It can be seen that isolated Fe_{W} point defect (white circle) and $3\text{Fe}_{\text{W}}\text{-S}$ associate (yellow triangle) indeed existed in the sample. The enlarged HAADF-STEM images of one Fe_{W} point defect marked with blue box and one $3\text{Fe}_{\text{W}}\text{-S}$ associate marked with red box in Fig. 5A are displayed in Fig. 5 (B and C), respectively. The contrast intensity profile in Fig. 5D measured along the blue broken line in Fig. 5A confirms that the Fe atom substitutes the W site, and the contrast intensity profile in Fig. 5E measured along the red broken line in Fig. 5A confirms that there is only single S atom at the center of the $3\text{Fe}_{\text{W}}\text{-S}$ associate. Similar to Fe-doped MoS_2 , Fe substitutes W randomly and the Fe doping concentration in monolayer Fe-doped WS_2 is ~ 4.6 at. % (fig. S17). Monolayer CVD-grown WS_2 is a well n-type semiconductor as reported widely (38, 39). Figure 5 (F and G) shows the output and transfer curves of monolayer Fe-doped WS_2 , showing good contact and a degenerate p-type property. This anomalous degenerate p-type semiconductor conductivity behavior suggests that $3\text{Fe}_{\text{W}}\text{-S}$ associates contributing holes to monolayer WS_2 , which is similar to that in monolayer Fe-doped MoS_2 .

Discussion

In this work, Fe_{Mo} point defects and $3\text{Fe}_{\text{Mo}}\text{-S}$ associates are fabricated and identified in CVD grown-monolayer Fe-doped MoS_2 . Combined STM/STS, electrical

transport measurements, and first-principles calculations confirm that Fe_{Mo} point defects act as electron donors, while $3\text{Fe}_{\text{Mo}}\text{-S}$ associates serve as hole donors, demonstrating that the same element dopant can induce distinct electronic behaviors dependent on the structural configurations. Moreover, similar $3\text{Fe}_{\text{W}}\text{-S}$ associates with hole doping properties are identified in monolayer Fe-doped WS_2 , indicating the generality of this mechanism. Our research explains why Fe-doped MoS_2 samples can present different electrical properties in previous studies, and highlights the potential of defect associates for tailoring the characteristics of 2D semiconductors.

Materials and Methods

Sample fabrication

Synthesis of monolayer Fe-doped MoS_2 : Monolayer Fe-doped MoS_2 flakes were fabricated using CVD method (fig. S1). A quartz boat containing 50 mg S powder (99.5%, Alfa Aesar A Johnson Matthey) was placed in the low temperature zone of the tubular furnace (upstream), and another quartz boat containing 1.5 mg NaCl (99.0%, Alfa Aesar A Johnson Matthey)/precursor mixture with a mass ratio of 9:1 was placed in the high temperature zone (downstream). Two kinds of precursors are used to prepare Fe-doped MoS_2 , one is $\text{Fe}_2\text{Mo}_3\text{O}_{12}$ (98.0%, Alab) and the other is MoO_3 (99.95%, Aladdin)/ FeS_2 (99.9%, Aladdin) mixture. A cleaned Si/ SiO_2 (oxide layer thickness:285 nm) wafer was positioned atop the quartz boat within the high-temperature zone to serve as the growth substrate. Before heating the tube furnace, N_2 with a flow rate of 400 standard cubic centimeter per minute (sccm) was introduced into the tube furnace for 10 min along the direction from the low to the high temperature zone to exhaust the air, and then the N_2 flow rate was adjusted to 150 sccm. The thermal protocol comprised three stages: (i) Ramping the high-temperature zone to 600 °C at 20 °C/min while initiating S powder heating in the low-temperature zone; (ii) Maintaining thermal gradients until the low-temperature zone reached 160 °C (achieved within 5 min) coinciding with high-temperature zone stabilizing at 700 °C, followed by 10 min isothermal growth for Fe-doped MoS_2 synthesis; (iii) Naturally cooling the furnace to

ambient temperature. The Fe doping concentration in monolayer MoS₂ can be tuned by controlling the mole ratio between FeS₂ and MoO₃ in precursor.

Synthesis of monolayer pristine MoS₂: It is the same with the synthesis of monolayer Fe-doped MoS₂ except that the precursor is replaced by pure MoO₃.

Synthesis of monolayer Fe-doped WS₂: It is the same with the synthesis of monolayer Fe-doped MoS₂ except that the precursor is replaced FeSO₄ • 7H₂O (≥99.0%, Xilong) /WO₃ (99.9%, Aladdin) mixture with 60 at.% Fe, and the growth is carried out at 800 °C for 3 min.

Atomic structure characterization of samples

All samples are transferred from the growth to the test substrates via water-assisted transfer method (40). All the TEM experiments were completed on the condenser Cs-STEM (FEI, Titan³ Themis Z) with 300 kV accelerating voltage.

STM/STS measurements

The monolayer Fe-doped MoS₂ flakes stacking on Au substrate were transferred into an ultrahigh vacuum (UHV) chamber of the STM system (USM-1300 from UNISOKU) and degassed at 300 °C for 4-6 hours with a pressure better than 3×10⁻¹⁰ Torr. The degassed sample was then transferred into a STM scanning chamber for *in situ* measurement in the UHV and low-temperature environment. All the STM measurements were performed at the constant-current mode and 77 K using an electrochemically etched tungsten tip. The *dI/dV* spectra were measured using a lock-in technique with a bias modulation amplitude of $V_{\text{mod}} = 10$ mV and frequency of 973.1 Hz.

Device fabrication

The FET devices were fabricated by electron beam lithography, electrodes deposition and lift-off processes. The electrodes are Ta (10 nm)/Pt (40 nm) deposited by magnetron sputtering.

First-principles calculations

The electronic structures of monolayer pristine and Fe-doped MoS₂ and the total energy calculations of all Fe-related configurations were performed by Vienna ab initio simulation package (VASP) (41, 42). The cutoff energy of 520 eV is taken for the plane-wave basis set (43). The exchange-correlation interactions are described by the generalized gradient approximation (GGA) with Perdew-Burke-Ernzerhof (PBE) type functional (44). Atoms are fully relaxed until the Hellmann-Feynman forces on each atom are less than 0.01 eV/Å. The first Brillouin zone sampling was performed using Γ -centered Monkhorst-Pack grids: a 3×3×1 mesh for lattice relaxation of the 4×4×1 supercell, followed by a higher-density 5×5×1 mesh for electronic structure determination. To mimic a 2D material, a layer distance of 20 Å along z direction is used to eliminate the interference between periodic images. The energy convergence threshold is established at 10⁻⁶ eV. Post-processing of data is carried out using VASPKIT code (45). Based on the force matrices from the first-principles calculations, the phonon modes of monolayer MoS₂ are carried out by the PHONOPY code (46, 47), where all atomic positions were fully optimized until the residual forces were less than 0.0001eV/Å.

Supplementary Materials

This PDF file includes:

Supplementary Text

Figs. S1 to S18

Table S1

References

References and Notes

1. B. Qin, C. Ma, Q. Guo, X. Li, W. Wei, C. Ma, Q. Wang, F. Liu, M. Zhao, G. Xue, J. Qi, M. Wu, H. Hong, L. Du, Q. Zhao, P. Gao, X. Wang, E. Wang, G. Zhang, C. Liu, K. Liu, Interfacial epitaxy of multilayer rhombohedral transition-metal dichalcogenide single crystals. *Science* **385**, 99-104 (2024).
2. D. Jayachandran, R. Pendurthi, M. U. K. Sadaf, N. U. Sakib, A. Pannone, C. Chen, Y. Han, N. Trainor, S. Kumari, T. V. Mc Knight, Three-dimensional integration of two-dimensional field-effect transistors. *Nature* **625**, 276-281

- (2024).
3. H. Ning, Z. Yu, Q. Zhang, H. Wen, B. Gao, Y. Mao, Y. Li, Y. Zhou, Y. Zhou, J. Chen, An in-memory computing architecture based on a duplex two-dimensional material structure for in situ machine learning. *Nat. Nanotechnol.* **18**, 493-500 (2023).
 4. K. M. Roccapiore, R. Torsi, J. Robinson, S. Kalinin, M. Ziatdinov, Dynamic STEM-EELS for single-atom and defect measurement during electron beam transformations. *Sci. Adv.* **10**, eadn5899 (2024).
 5. T. Li, J. Miao, X. Fu, B. Song, B. Cai, X. Ge, X. Zhou, P. Zhou, X. Wang, D. Jariwala, W. Hu, Reconfigurable, non-volatile neuromorphic photovoltaics. *Nat. Nanotechnol.* **18**, 1303-1310 (2023).
 6. F. Xiang, L. Huberich, P. A. Vargas, R. Torsi, J. Allerbeck, A. M. Z. Tan, C. Dong, P. Ruffieux, R. Fasel, O. Gröning, Y.-C. Lin, R. G. Hennig, J. A. Robinson, B. Schuler, Charge state-dependent symmetry breaking of atomic defects in transition metal dichalcogenides. *Nat. Commun.* **15**, 2738 (2024).
 7. J. Jiang, L. Xu, L. Du, L. Li, G. Zhang, C. Qiu, L.-M. Peng, Yttrium-doping-induced metallization of molybdenum disulfide for ohmic contacts in two-dimensional transistors. *Nat. Electron.* **7**, 545-556 (2024).
 8. H. Li, J. Yang, X. Li, Q. Luo, M. Cheng, W. Feng, R. Du, Y. Wang, L. Song, X. Wen, Y. Wen, M. Xiao, L. Liao, Y. Zhang, J. Shi, J. He, Bridging synthesis and controllable doping of monolayer 4 in. length transition-metal dichalcogenides single crystals with high electron mobility. *Adv. Mater.* **35**, 2211536 (2023).
 9. Y. Tan, S.-H. Yang, C.-P. Lin, F. J. Vega, J. Cai, H.-Y. Lan, R. Tripathi, S. Sharma, Z. Shang, T.-H. Hou, Monolayer WSe₂ field-effect transistor performance enhancement by atomic defect engineering and passivation. *ACS Nano* **19**, 8916-8925 (2025).
 10. J. Xu, X.-X. Xue, G. Shao, C. Jing, S. Dai, K. He, P. Jia, S. Wang, Y. Yuan, J. Luo, J. Lu, Atomic-level polarization in electric fields of defects for electrocatalysis. *Nat. Commun.* **14**, 7849 (2023).
 11. C. Lei, Z. Qian, Y. Ma, R. Ahuja, What is the role of a magnetic Mo antisite defect on carrier relaxation and spin dynamics in 2-D MoS₂? *Nano Lett.* **25**, 7378-7384 (2025).
 12. S. Li, X. Zhao, T. Wang, J. Wu, X. Xu, P. Li, X. Ji, H. Hou, X. Qu, L. Jiao, Unraveling the "gap-filling" mechanism of multiple charge carriers in aqueous Zn-MoS₂ batteries. *Angew. Chem. Inter. Ed.* **63**, e202320075 (2024).
 13. R. D. Septianto, A. P. Romagosa, Y. Dong, H. Matsuoka, T. Ideue, Y. Majima, Y. Iwasa, Gate-controlled potassium intercalation and superconductivity in molybdenum disulfide. *Nano Lett.* **24**, 13790-13795 (2024).
 14. Y. Lei, D. Butler, M. C. Lucking, F. Zhang, T. Xia, K. Fujisawa, T. Granzier-Nakajima, R. Cruz-Silva, M. Endo, H. Terrones, M. Terrones, A. Ebrahimi, Single-atom doping of MoS₂ with manganese enables ultrasensitive detection of dopamine: Experimental and computational approach. *Sci. Adv.* **6**, eabc4250 (2020).
 15. A. Kozhakhmetov, B. Schuler, A. M. Z. Tan, K. A. Cochrane, J. R. Nasr, H. El-

- Sherif, A. Bansal, A. Vera, V. Bojan, J. M. Redwing, Scalable substitutional Redoping and its impact on the optical and electronic properties of tungsten diselenide. *Adv. Mater.* **32**, 2005159 (2020).
16. M. Das, D. Sen, N. U. Sakib, H. Ravichandran, Y. Sun, Z. Zhang, S. Ghosh, P. Venkatram, S. Subbulakshmi Radhakrishnan, A. Sredenschek, High-performance p-type field-effect transistors using substitutional doping and thickness control of two-dimensional materials. *Nat. Electron.* **8**, 24-35 (2025).
 17. K. Ko, J. Huang, J. Kwon, M. Jang, H. Cho, S. Yang, S. Kim, S. Park, T. Taniguchi, K. Watanabe, Competition between bipolar conduction modes in extrinsically p-doped MoS₂: Interaction with gate dielectric matters. *ACS Nano* **19**, 1630-1641 (2024).
 18. L. Yu, J. Tan, H. Ma, B. Liu, F. Kang, R. Lv, Large-area monolayer p-type semiconductor films toward high-performance electrical device arrays. *Adv. Mater.* e00886 (2025) (DOI: 10.1002/adma.202500886).
 19. H. Li, M. Cheng, P. Wang, R. Du, L. Song, J. He, J. Shi, Reducing contact resistance and boosting device performance of monolayer MoS₂ by in-situ Fe doping. *Adv. Mater.* **34**, 2200885 (2022).
 20. J. Yang, L. Huang, H. Li, X. Li, L. Song, Y. Peng, R. Xu, X. Wen, H. Sun, Y. Jiang, J. He, J. Shi, Understanding iron-doping modulating domain orientation and improving the device performance of monolayer molybdenum disulfide. *Nano Lett.* **24**, 12866-12873 (2024).
 21. S. Y. Wang, T. S. Ko, C. C. Huang, D. Y. Lin, Y. S. Huang, Optical and electrical properties of MoS₂ and Fe-doped MoS₂. *Jap. J. Appl. Phys.* **53**, 04EH07 (2014).
 22. B. Tang, Z. G. Yu, H. L. Seng, N. Zhang, X. Liu, Y.-W. Zhang, W. Yang, H. Gong, Simultaneous edge and electronic control of MoS₂ nanosheets through Fe doping for an efficient oxygen evolution reaction. *Nanoscale* **10**, 20113-20119 (2018).
 23. R. Tao, Z.-H. Yang, C. Tan, X. Hao, Z.-G. Ke, L. Yang, L.-P. Dai, X.-W. Deng, P.-J. Li, Z.-G. Wang, Growth of Fe-doped and V-doped MoS₂ and their magnetic-electrical effects. *J. Electron. Sci. Technol.* **20**, 100167 (2022).
 24. H. Li, Q. Zhang, C. C. R. Yap, B. K. Tay, T. H. T. Edwin, A. Olivier, D. Baillargeat, From bulk to monolayer MoS₂: Evolution of Raman scattering. *Adv. Funct. Mater.* **22**, 1385-1390 (2012).
 25. X. Zhang, X.-F. Qiao, W. Shi, J.-B. Wu, D.-S. Jiang, P.-H. Tan, Phonon and Raman scattering of two-dimensional transition metal dichalcogenides from monolayer, multilayer to bulk material. *Chem. Soc. Rev.* **44**, 2757-2785 (2015).
 26. E. V. Miu, J. R. McKone, G. Mpourmpakis, The sensitivity of metal oxide electrocatalysis to bulk hydrogen intercalation: Hydrogen evolution on tungsten oxide. *J. Am. Chem. Soc.* **144**, 6420-6433 (2022).
 27. P. D. Nellist, S. J. Pennycook, Direct imaging of the atomic configuration of ultradispersed catalysts. *Science* **274**, 413-415 (1996).
 28. C. T. Koch, Determination of core structure periodicity and point defect density along dislocations, PhD thesis, *Arizona State University* (2002).
 29. N. Krane, C. Lotze, J. M. Läger, G. Reece, K. J. Franke, Electronic structure

- and luminescence of quasi-freestanding MoS₂ nanopatches on Au (111). *Nano Lett.* **16**, 5163-5168 (2016).
30. S. G. Sørensen, H. G. Fächtbauer, A. K. Tuxen, A. S. Walton, J. V. Lauritsen, Structure and electronic properties of in situ synthesized single-layer MoS₂ on a gold surface. *ACS Nano* **8**, 6788-6796 (2014).
 31. W. Li, J. Huang, B. Han, C. Xie, X. Huang, K. Tian, Y. Zeng, Z. Zhao, P. Gao, Y. Zhang, Molten-salt-assisted chemical vapor deposition process for substitutional doping of monolayer MoS₂ and effectively altering the electronic structure and phononic properties. *Adv. Sci.* **7**, 2001080 (2020).
 32. Y. Bao, J. Shao, H. Xu, J. Yan, P.-T. Jing, J. Xu, D. Zhan, B. Li, K. Liu, L. Liu, D. Shen, Making patterned single defects in MoS₂ thermally with the MoS₂/Au Moiré Interface. *ACS Nano* **18**, 27411-27419 (2024).
 33. S. M. Hus, R. Ge, P.-A. Chen, L. Liang, G. E. Donnelly, W. Ko, F. Huang, M.-H. Chiang, A.-P. Li, D. Akinwande, Observation of single-defect memristor in an MoS₂ atomic sheet. *Nat. Nanotechnol.* **16**, 58-62 (2021).
 34. M. Liu, Y. Li, X. Zhou, D. Ma, Y. Qi, Y. F. Zhang, Z. Liu, Temperature-triggered sulfur vacancy evolution in monolayer MoS₂/graphene heterostructures. *Small* **13**, 1602967 (2017).
 35. D. Y. Qiu, F. H. Da Jornada, S. G. Louie, Optical spectrum of MoS₂: many-body effects and diversity of exciton states. *Phys. Rev. Lett.* **111**, 216805 (2013).
 36. J. A. Miwa, S. Ulstrup, S. G. Sørensen, M. Dendzik, A. G. Čabo, M. Bianchi, J. V. Lauritsen, P. Hofmann, Electronic structure of epitaxial single-layer MoS₂. *Phys. Rev. Lett.* **114**, 046802 (2014).
 37. K. F. Mak, C. Lee, J. Hone, J. Shan, T. F. Heinz, Atomically thin MoS₂: a new direct-gap semiconductor. *Phys. Rev. Lett.* **105**, 136805 (2010).
 38. A. Sebastian, R. Pendurthi, T. H. Choudhury, J. M. Redwing, S. Das, Benchmarking monolayer MoS₂ and WS₂ field-effect transistors. *Nat. Commun.* **12**, 693 (2021).
 39. Y. Cui, R. Xin, Z. Yu, Y. Pan, Z. Y. Ong, X. Wei, J. Wang, H. Nan, Z. Ni, Y. Wu, High-performance monolayer WS₂ field-effect transistors on high- κ dielectrics. *Adv. Mater.* **27**, 5230-5234 (2015).
 40. L. Zhang, C. Wang, X.-L. Liu, T. Xu, M. Long, E. Liu, C. Pan, G. Su, J. Zeng, Y. Fu, Y. Wang, Z. Yan, A. Gao, K. Xu, P.-H. Tan, L. Sun, Z. Wang, X. Cui, F. Miao, Damage-free and rapid transfer of CVD-grown two-dimensional transition metal dichalcogenides by dissolving sacrificial water-soluble layers. *Nanoscale* **9**, 19124-19130 (2017).
 41. G. Kresse, J. Furthmüller, Efficient iterative schemes for ab initio total-energy calculations using a plane-wave basis set. *Phys. Rev. B* **54**, 11169-11186 (1996).
 42. G. Kresse, J. Hafner, Ab initio molecular-dynamics simulation of the liquid-metal-amorphous-semiconductor transition in germanium. *Phys. Rev. B* **49**, 14251-14269 (1994).
 43. P. E. Blöchl, Projector augmented-wave method. *Phys. Rev. B* **50**, 17953 (1994).
 44. J. P. Perdew, K. Burke, M. Ernzerhof, Generalized gradient approximation made simple. *Phys. Rev. Lett.* **77**, 3865-3868 (1996).

45. V. Wang, N. Xu, J.-C. Liu, G. Tang, W.-T. Geng, VASPKIT: A user-friendly interface facilitating high-throughput computing and analysis using VASP code. *Comput. Phys. Commun.* **267**, 108033 (2021).
46. A. Togo, L. Chaput, T. Tadano, I. Tanaka, Implementation strategies in phonopy and phono3py. *J. Phys.: Condens. Matter* **35**, 353001 (2023).
47. A. Togo, First-principles phonon calculations with phonopy and phono3py. *J. Phys. Soc. Jpn.* **92**, 012001 (2023).
48. A. Stacy, D. Hodul, Raman spectra of IVB and VIB transition metal disulfides using laser energies near the absorption edges. *J. Phys. Chem. Solids* **46**, 405-409 (1985).
49. Q. Zhang, L. Zhang, C. Jin, Y. Wang, F. Lin, CalAtom: A software for quantitatively analysing atomic columns in a transmission electron microscope image. *Ultramicroscopy* **202**, 114-120 (2019).

Acknowledgements

We thank Xuegang Chen and Mingsheng Long at Anhui University for their assistance in electrical characterizations.

Funding:

This work was supported by the Natural Science Foundation of Gansu Province (24JRRA398), the Excellent Doctoral Student Program of Gansu Province (23JRRA1130 and 25JRRA741), the Open Fund of Information Materials and Intelligent Sensing Laboratory of Anhui Province (IMIS202301), the Project of Yunnan Key Laboratory of Electromagnetic Materials and Devices, Yunnan University (ZZ2024007), the Gansu Youth Science and Technology Fund (23JRRA624), and the National Natural Science Foundation of China (62104089, 12274185, 12474128, 12204008 and 12104004).

Author contributions: L.Z. and Y.P. conceived the whole project. X.Q., J.Z. and L.Z. designed the experiments, prepared and characterized the samples, analyzed and interpreted the main data. X.Q., X.Y., Z.Z., and L.S. finished the STM/STS measurements and analyzed corresponding data. X.Q., X.P., H.M. D.G., A.Z. and M.S. performed the Raman spectra collection, DFT and first-principles calculations. C.Y., H.Z. and Y.W. assisted in the electrical characterizations of samples. H.L. assisted in the AFM characterizations. X.Q., L.Z., Z.Z., H.M., M.S. and Y.P. co-wrote the manuscript, and all authors commented on the manuscript.

Competing interests: The authors declare no competing interests.

Data and materials availability: The data that support the findings of this study are available from the corresponding authors upon reasonable request.

Figures:

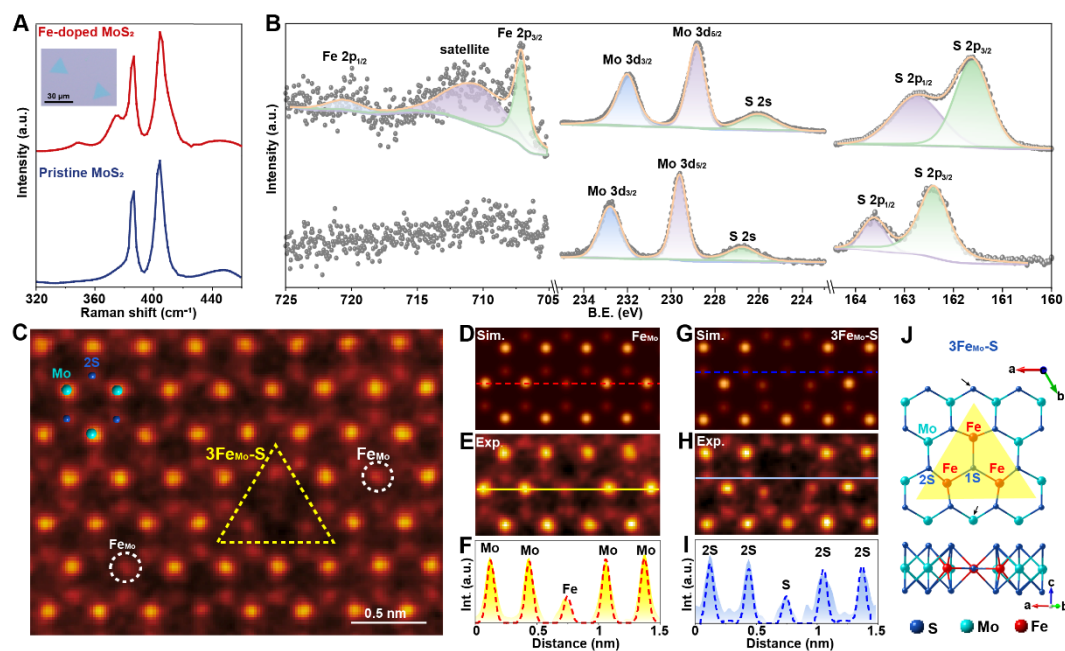


Fig. 1. Characterizations of monolayer Fe-doped and pristine MoS₂. (A) Raman spectra of monolayer Fe-doped and pristine MoS₂, the inset in (A) shows the optical image of freshly prepared monolayer Fe-doped MoS₂ flakes. (B) Fine scanning Fe 2p, Mo 3d, and S 2p XPS spectra of Fe-doped and pristine MoS₂. (C) Atomic scale HAADF-STEM image of monolayer Fe-doped MoS₂, white circle and yellow triangle respectively indicate Fe_{Mo} point defect and 3Fe_{Mo}-S associate. The atomic images (D and G) simulated by QSTEM software and (E and H) taken experimentally. (F and I) The contrast intensity curves measured along the broken and solid lines marking the atomic positions in (D and E) and (G and H) respectively. (J) Schematic diagram of the atomic structure of one 3Fe_{Mo}-S defect associate, and the yellow triangle marks the main part of the associate. Blue, cyan, and red spheres denote S, Mo, and Fe atoms, respectively. The S and Mo atoms marked with arrows in the top view are hidden in the side view in order to observe the 3Fe_{Mo}-S configuration more clearly.

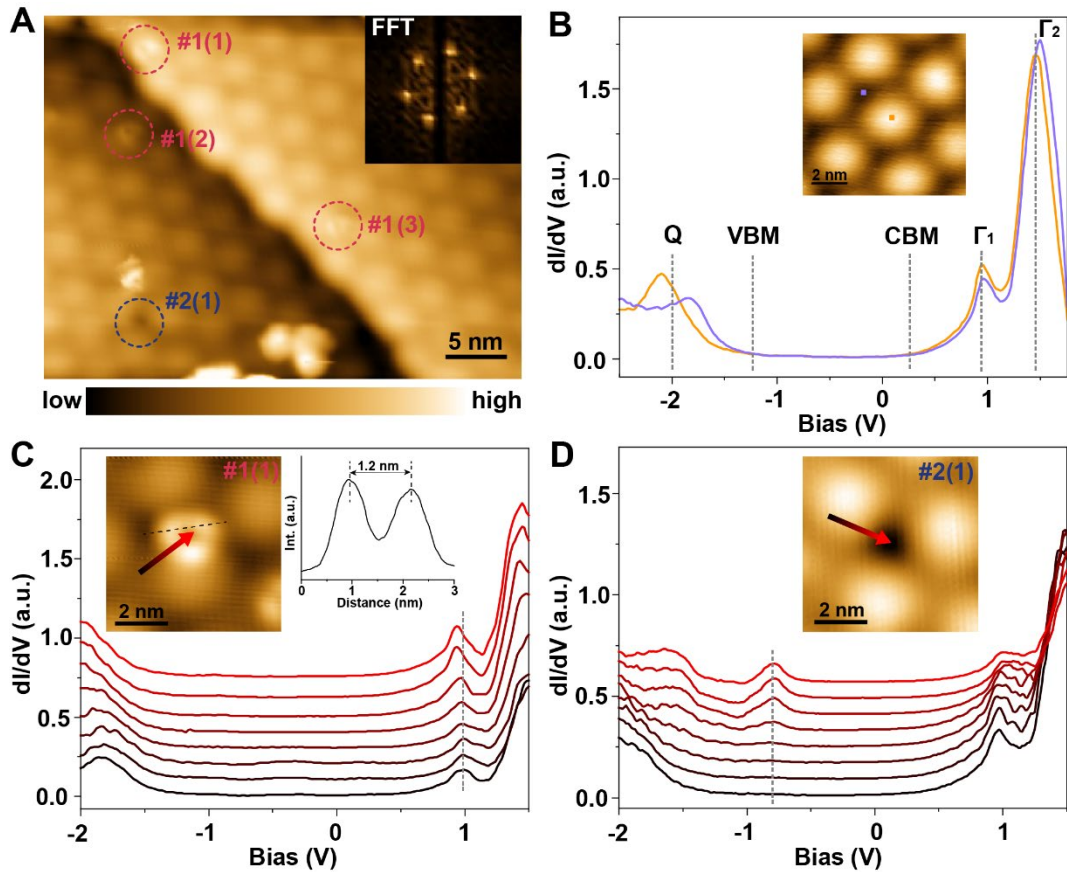


Fig. 2. STM/STS characterizations of isolated FeM₀ point defects and 3FeM₀-S associates. (A) A STM image of monolayer Fe-doped MoS₂ stacking on Au (111) substrate and its corresponding FFT image (inset) ($V_{\text{set}} = -0.8$ V, $I_{\text{set}} = 30$ pA). (B) dI/dV spectra measured on the top (orange point) and hollow (purple point) regions on pristine MoS₂ monolayer. A series of STS spectra measured along the arrow direction approaching the center of (C) an isolated FeM₀ point defect and (D) a 3FeM₀-S associate. Spectra are vertically shifted for clarity. The curve in the right inset of (C) is the contrast intensity curve measured along the black broken line in the left inset of (C). All spectra are measured at the setpoint of $V_{\text{set}} = -2$ V, $I_{\text{set}} = 300$ pA and at the temperature of $T = 77$ K.

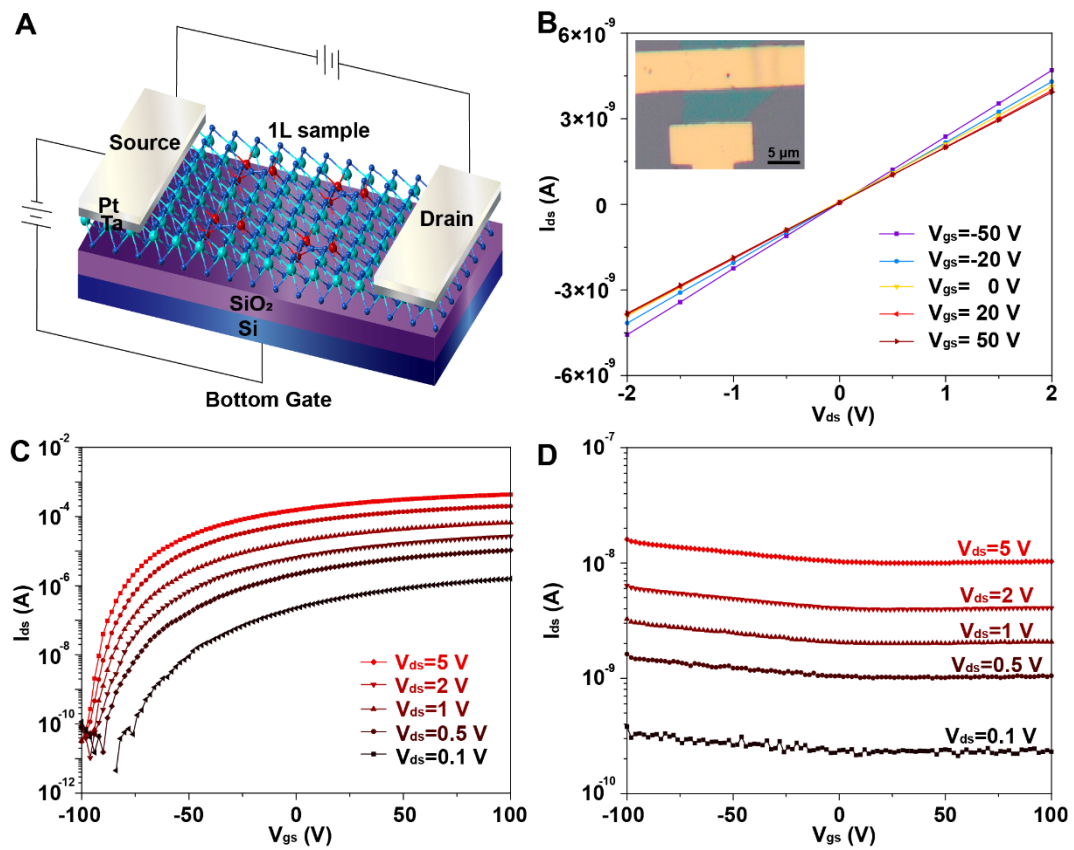


Fig. 3. Electrical transport properties of monolayer pristine and Fe-doped MoS₂. (A) Schematic diagram of the monolayer Fe-doped MoS₂ FET device. (B) The output curves of monolayer Fe-doped MoS₂ and the optical image of a practical device (inset). The transfer curves of monolayer (C) pristine MoS₂ and (D) Fe-doped MoS₂.

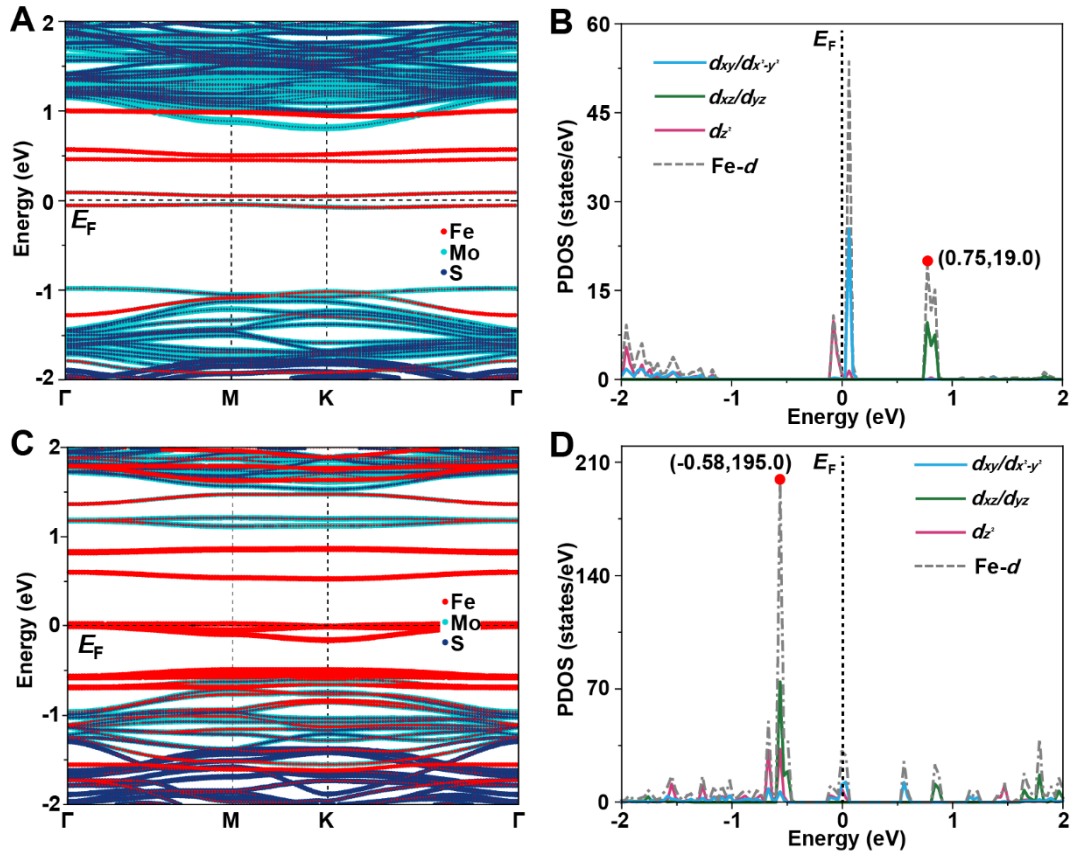


Fig. 4. Calculated electronic structures of monolayer pristine and Fe-doped MoS₂. Band structure of monolayer MoS₂ (A) containing one isolated Fe_{M0} point defect and (C) containing one 3Fe_{M0}-S associate. The red, cyan, and dark blue dots represent the contribution of Fe, Mo, and S atoms in monolayer Fe-doped MoS₂, respectively. PDOS of monolayer MoS₂ (B) containing one isolated Fe_{M0} point defect and (D) containing one 3Fe_{M0}-S associate. The blue, green, and pink solid lines represent the contribution of $d_{xy}/d_{x^2-y^2}$, d_{xz}/d_{yz} and d_{z^2} orbitals of Fe in Fe-doped MoS₂, respectively, and the gray dotted line indicates their overall contribution.

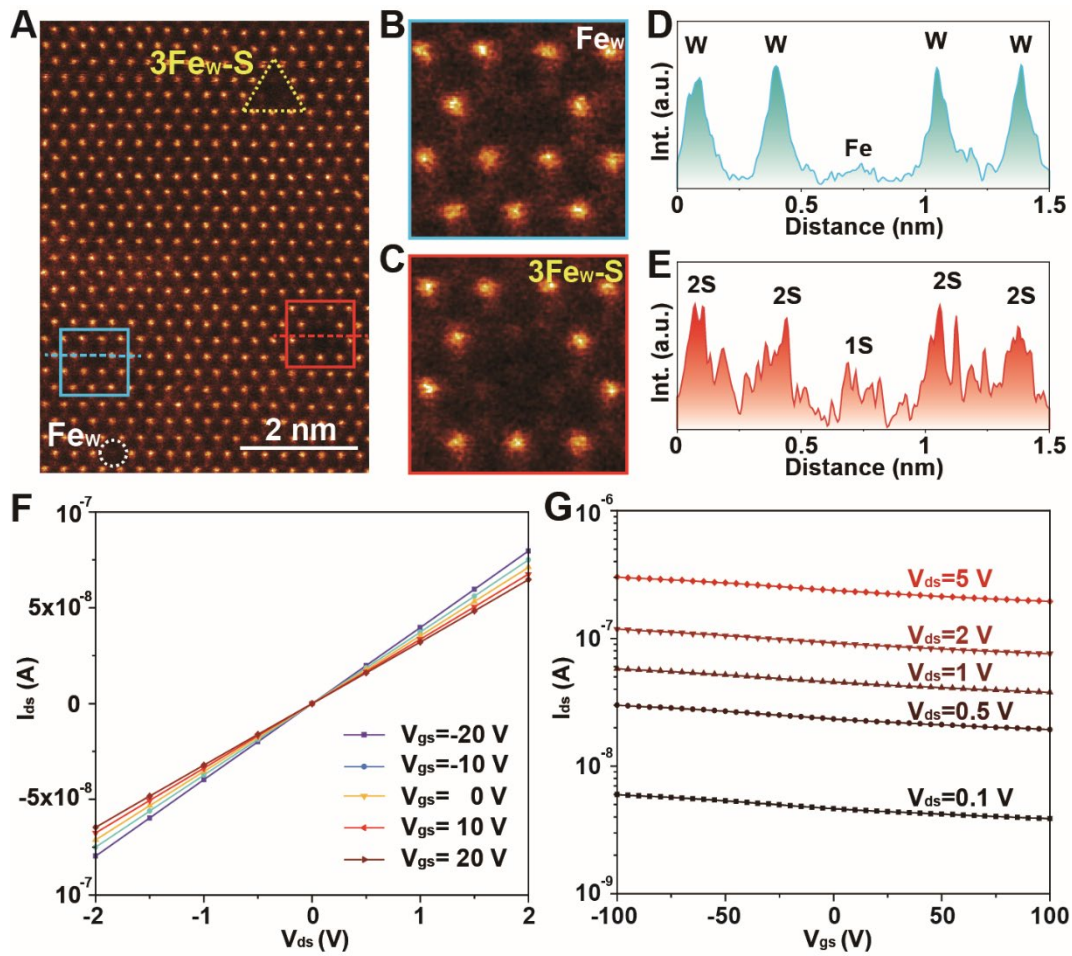


Fig. 5. Atomic structure and electrical transport properties of monolayer Fe-doped WS₂. (A) Atomic-scale HAADF-STEM image of monolayer Fe-doped WS₂. Two kinds of defects: (B) isolated Fe_w point defect and (C) 3Fe_w-S defect associate enlarged from the positions of blue and red rectangle in (A). (D), The intensity profile of the atomic positions marked with blue broken line of Fe and its nearby W site at the blue rectangle in (A). (E) The intensity profile of the atomic positions marked with red broken line of S and its nearby S₂ site at the red rectangle in (A). (F) The output curves and (G) the transfer curves of monolayer Fe-doped WS₂.

Supplementary Materials for

**Origin of anomalous p-type conductivity in
monolayer Fe-doped MoS₂**

Xiangning Quan *et al.*

*Lili Zhang, zll@lzu.edu.cn; Anmin Zhang, amzhang@lzu.edu.cn; Zongyuan Zhang, zongyuanzhang@ahu.edu.cn; Yong Peng, pengy@lzu.edu.cn

This PDF file includes:

Supplementary Text
Figs. S1 to S17
Table S1
References 48 and 49

Supplementary Text

1. Collection and analysis of the Raman spectra of monolayer Fe-doped MoS₂

Raman spectra of monolayer Fe-doped MoS₂ were collected with a LABRAM HR Evolution system at room temperature, which is equipped with a single grating of 800 mm focus length and liquid-nitrogen-cooled CCD. A laser with a wavelength of 532 nm was focused on the surface of monolayer pristine and Fe-doped MoS₂ flakes, and the excitation laser power was kept less than 0.3 mW to avoid heating effect. Here, we use the Porto notation $k_i (e_i, e_s) k_s$, where k_i and k_s denote the direction of incident and scattered light and (e_i, e_s) are their polarization, respectively. x, y and z correspond to the laboratory Cartesian coordinate system, with the z axis parallel to the c axis of sample. An angle-dependent Raman was performed with the polarization configuration $z(yy)\bar{z}$ and the z direction as the axis. The sample was rotated from 0° to 180° by taking 10° as the step to record the Raman peak intensities, complete all results from 0° to 360° by angle symmetry.

In Raman spectroscopy, the Raman scattering intensity can be expressed as $I \propto |\vec{e}_i \cdot \vec{M} \cdot \vec{R} \cdot \vec{M}^{-1} \cdot \vec{e}_s|^2$, where \vec{e}_i is the polarization vector of the incident light, \vec{e}_s is the polarization vector of the scattered light, and \vec{M} is the transformation matrix relating with the crystal coordinate to the laboratory coordinate. If the angle between the two coordinate systems is θ , \vec{M} can be expressed as $\vec{M} = \begin{pmatrix} \cos\theta & \sin\theta & 0 \\ -\sin\theta & \cos\theta & 0 \\ 0 & 0 & 1 \end{pmatrix}$

in our experiment. The Raman tensor \vec{R} is determined by the symmetry of the crystal. Therefore, by rotating the sample and performing Raman measurements at regular angular intervals, the function relationship between the integrated Raman intensity and θ can be used to determine the Raman tensor and identify the Raman peaks. Figure S3A shows the polarized Raman spectra of monolayer Fe-doped MoS₂. Besides the two main first-order bands E' mode (in-plane vibration of S and Mo atoms, referred as E_{2g}¹ in even layer sample or bulk) and A₁' mode (out-of-plane vibration of S atoms, referred as A_{1g} in even layer sample or bulk) around 385.1 cm⁻¹ and 404.5 cm⁻¹, Raman peaks also arise at 349.4 cm⁻¹, 375.8 cm⁻¹, and around 455 cm⁻¹. The Raman peak locating at

455 cm^{-1} is commonly called the 2LA band of MoS_2 (48). Monolayer pristine MoS_2 has six optical phonon modes, the frequencies of the other four optical phonon modes are significantly away from 349.4 cm^{-1} and 375.8 cm^{-1} , which are marked as P_1 and P_2 later, respectively. To identify P_1 and P_2 , phonon spectra calculations and symmetry analysis were performed on monolayer pristine MoS_2 as shown in fig. S3B and Table S1.

Angle-resolved polarized Raman spectra were performed on monolayer Fe-doped MoS_2 samples under $z(yy)\bar{z}$ polarization configuration and the results are shown in fig. S3C. The integrated Raman intensities of P_1 , P_2 , E' and A_1' modes under the $z(yy)\bar{z}$ polarization configuration were fitted with Lorentzian curve, and the results are shown in fig. S3 (D to G). For E' and A_1' displayed in fig. S3 (D and E), the integrated intensities are approximately isotropic at all polarization angles, consistent with their Raman tensors corresponding to their irreducible representations. The integrated intensities of P_1 and P_2 are also approximately isotropic as shown in fig. S3 (F and G), which corresponds to the Raman tensors of $A_1'(K)$ and $A_1(M)$, respectively (when the xx and yy diagonal elements of the $A_1(M)$ Raman matrix are approximately equal). Combined with the calculated phonon frequencies at the M and K points, P_1 can be attributed to $A_1(M)$ at 340.1 cm^{-1} , and P_2 can be assign to $A_1(M)$ or $A_1'(K)$ at 390.7 cm^{-1} .

2. The total energy of 3Fe_{M0}-S associate with the position of central S atom.

It is found that the position of S atom along the normal line of the equilateral triangle formed by three Fe atoms plays a key role in determining the total energy of 3Fe_{M0}-S associate. Setting the total energy of the system to be 0 eV upon S at central position, the total energy difference (ΔE) shown in fig. S10 demonstrates that ΔE is changed with the S position along the normal line of the triangle. ΔE gets the minimum when the central S atom is coplanar with its neighboring Fe atoms, suggesting that 3Fe_{M0}-S associate prefers to be a planar structure.

3. The calculation method for Fe doping concentration.

Figure S7 (A and D) shows the atomic HADDF-STEM image of monolayer pristine and Fe-doped MoS₂ along the [0001] direction, respectively. All enlarged atomic diagrams in Fig. 1 (C, E and H) in the main text are taken from the corresponding positions in fig. S7D and are marked with white, yellow, and blue boxes, respectively. All Mo sites and Fe sites in fig. S7 (A and D) are labelled as cyan and red circles respectively by CalAtom software (49) according to the Z-contrast of different atoms, and the results are shown in fig. S7 (B and E), respectively. The Fe_{Mo} point defects and the 3Fe_{Mo}-S associates can be clearly seen in fig. S7E and the 3Fe_{Mo}-S associates are marked with red triangles. After analyzing the contrast intensity distribution of all labelled spots in fig. S7E, the contrast intensity distribution splits into two Gaussian peaks. One is located at lower intensity range and the other locates at higher intensity range, which correspond to Fe sites and Mo sites, respectively. By calculating the number of atoms belonging to these two peaks with different brightness, the doping concentration of Fe can be determined to be 6.9 at.%. Accordingly, the analyzing result of fig. S7B only shows one peak as shown in fig. S7C since there are only Mo atoms in the metal sites.

4. Calculation of the formation energy for different Fe-related defect configurations in monolayer Fe-doped MoS₂.

Four different Fe-related defect configurations are considered, which are named Fe_{Mo} point defect, 3Fe_{Mo}-S associate, 3Fe_{Mo} (I) and 3Fe_{Mo} (II), respectively. 3Fe_{Mo} (I) represents the configuration of 3Fe_{Mo} associate with two S atoms still remain in the center, and 3Fe_{Mo} (II) represents the configuration of 3Fe_{Mo} associate consisting of three adjacent Fe atoms without central S atoms. Figure S11 shows the top views and side views of these four defect configurations.

The formation energies of above defect configurations are calculated using the following formula:

$$E_f = E_{\text{def}} - E_{\text{host}} + \sum_i n_i u_i,$$

where E_{def} is the total energy of Fe-doped MoS₂ and E_{host} is that of host MoS₂. Both energies are calculated based on 4×4×1 supercell. n_i is the number of increase ($n_i < 0$) or decrease ($n_i > 0$) atom, and u_i denotes the chemical potential of atomic number n_i . Naturally, we can respectively write out the concrete expressions of the formation energies for these four defect configurations:

Fe_{Mo}:

$$E_f = E_{\text{def}} - E_{\text{host}} + u_{\text{Mo}} - u_{\text{Fe}}$$

3Fe_{Mo}-S:

$$E_f = E_{\text{def}} - E_{\text{host}} + 3u_{\text{Mo}} + u_{\text{S}} - 3u_{\text{Fe}}$$

3Fe_{Mo} (I):

$$E_f = E_{\text{def}} - E_{\text{host}} + 3u_{\text{Mo}} - 3u_{\text{Fe}}$$

3Fe_{Mo} (II):

$$E_f = E_{\text{def}} - E_{\text{host}} + 3u_{\text{Mo}} - 3u_{\text{Fe}}.$$

Under S-rich condition, u_{Fe} is half of the energy calculated in Fe cubic bulk, i.e. $u_{\text{Fe}} = 0.5E_{\text{Fe}}$, and $u_{\text{S}} = 0.125E_{\text{S}_8}$ with E_{S_8} being the energy of one S₈ molecule. Then, $u_{\text{Mo}} = E_{\text{MoS}_2} - 2u_{\text{S}}$, where E_{MoS_2} is the total energy of MoS₂ conventional unit cell. Thus, the formation energies of Fe_{Mo} point defect, 3Fe_{Mo}-S associate, 3Fe_{Mo} (I) and 3Fe_{Mo} (II) are 0.10 eV, 1.03 eV, 2.52 eV and 3.75 eV, respectively, which are shown in fig. S12.

Fig. S1.

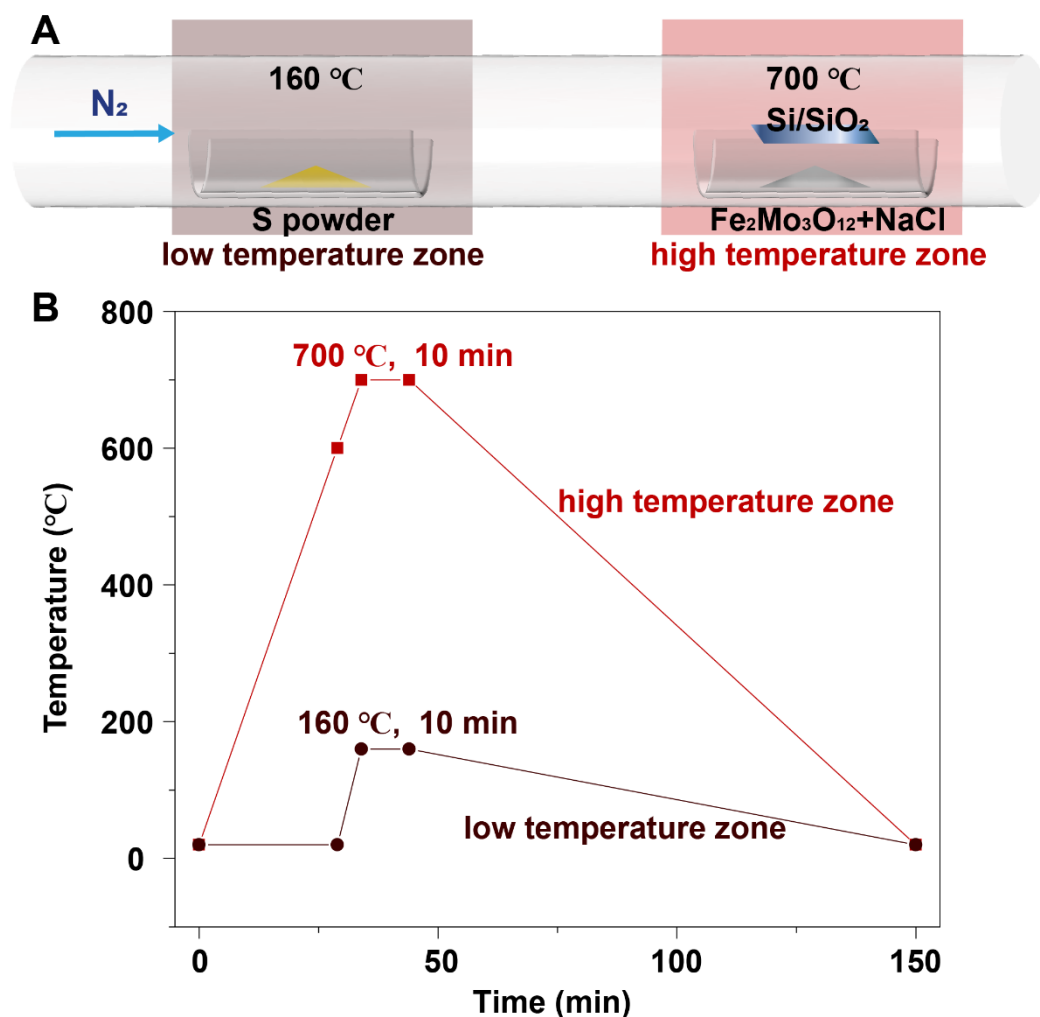


Fig. S1. Synthesis of monolayer Fe-doped MoS₂. (A) Schematic diagram for CVD fabrication of monolayer Fe-doped MoS₂. (B) Time-temperature control curve of each temperature zone in the synthesis process.

Fig. S2.

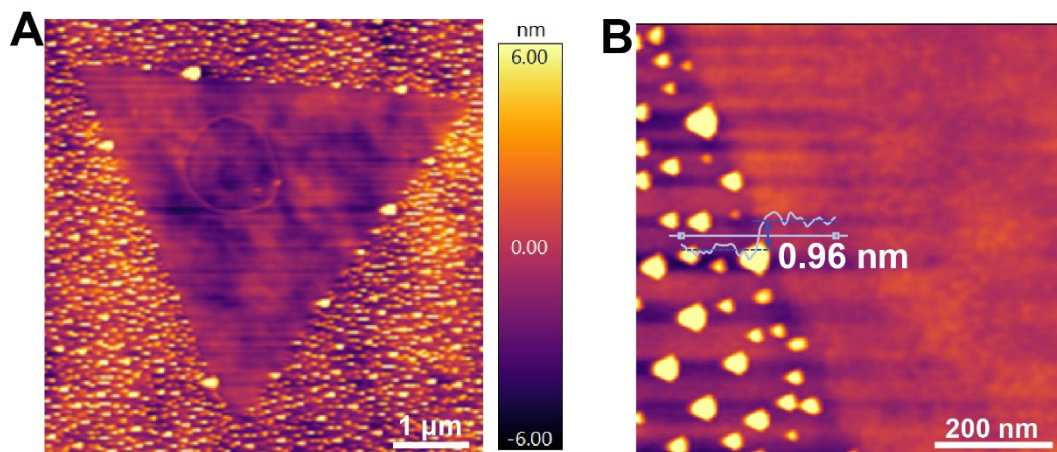


Fig. S2. Atomic force microscopy (AFM) characterization of monolayer Fe-doped MoS₂. (A) AFM image of a freshly prepared monolayer Fe-doped MoS₂ flake. (B) The height profile along the white line across the flake edge measured by AFM.

Fig. S3.

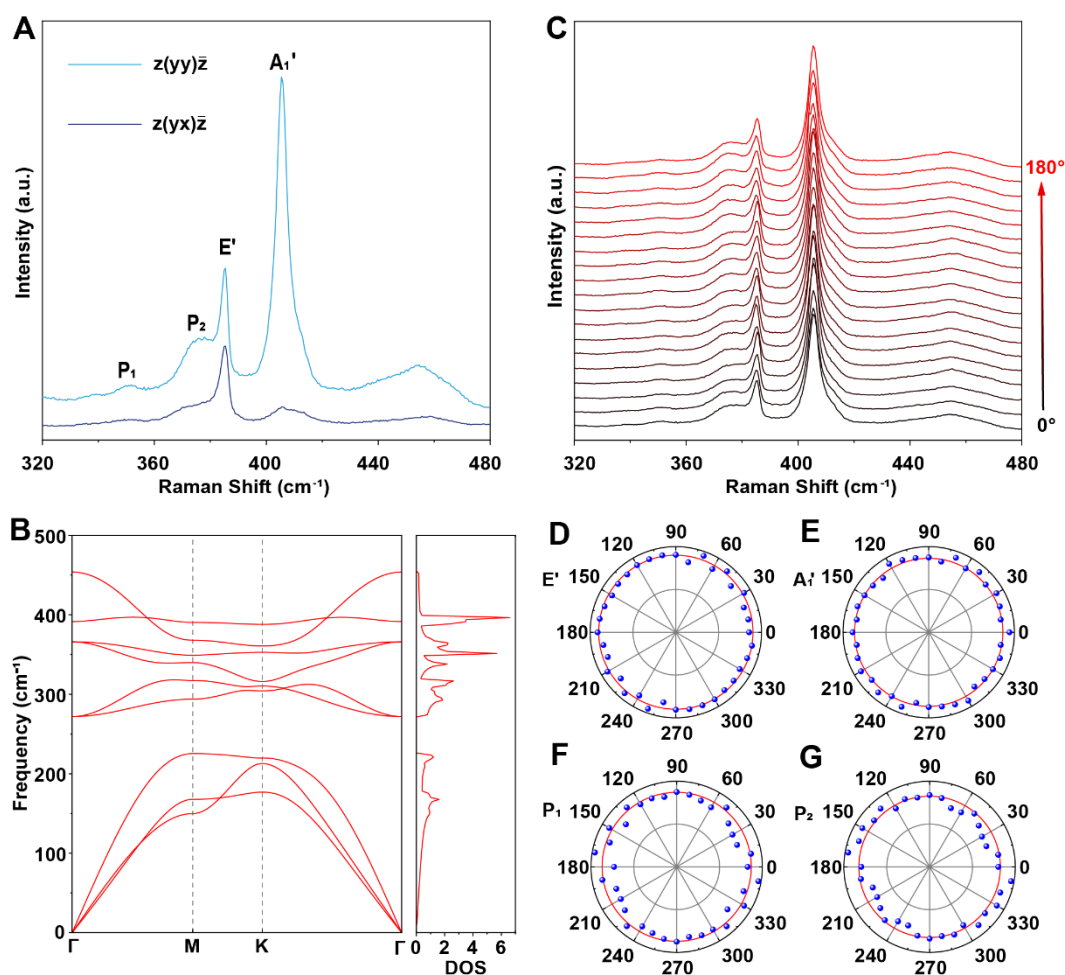


Fig. S3. Raman spectra of monolayer Fe-doped MoS₂. (A) Polarized Raman spectra of monolayer Fe-doped MoS₂. (B) Phonon dispersion and vibrational density of states (DOS) of monolayer MoS₂ calculated from density functional theory (DFT) calculation. (C) Angle-resolved polarized Raman spectra of monolayer Fe-doped MoS₂ from 0° to 180°. (D to G) Polar plots for the spectrally integrated intensities of E', A₁', P₁, and P₂ phonons as a function of incident polarization angle θ .

Fig. S4.

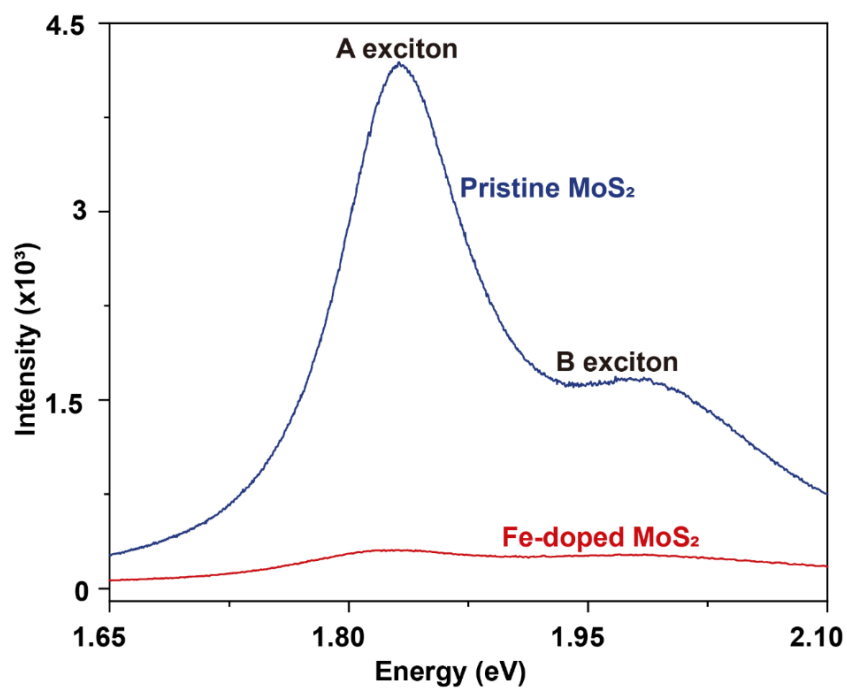


Fig. S4. Photoluminescence (PL) spectra of monolayer Fe-doped and pristine MoS₂. Pristine MoS₂ displays two peaks at 1.83 eV (A exciton) and 1.98 eV (B exciton). Incorporation of Fe atoms leads to a strong quenching effect of PL in monolayer Fe-doped MoS₂.

Fig. S5.

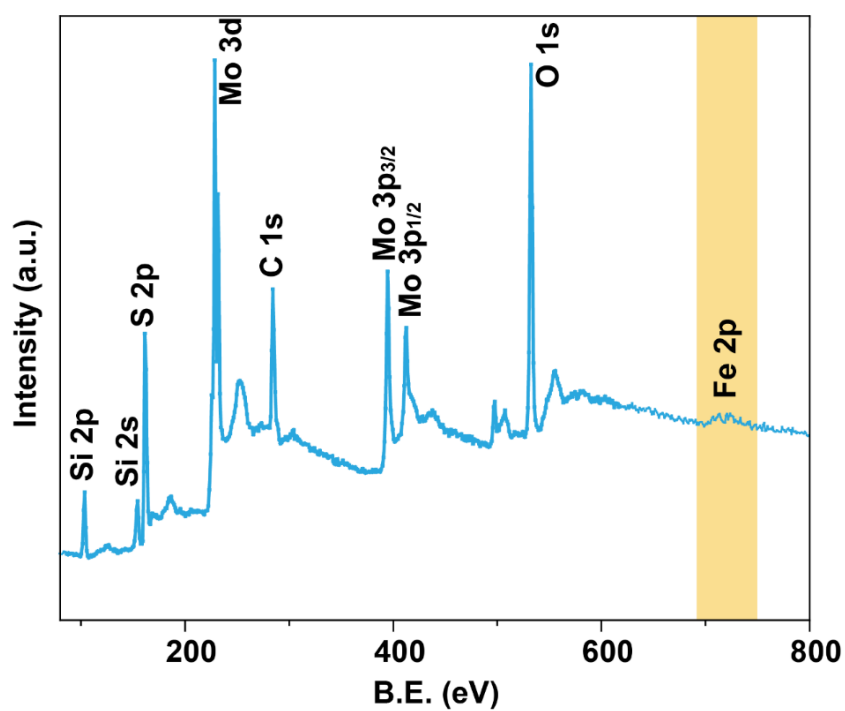


Fig. S5. Survey XPS spectrum of as-grown Fe-doped MoS₂ on Si/SiO₂ substrate.

The XPS peaks of Si (103.4 eV, 153.3 eV) and O (532.9 eV) come from the Si/SiO₂ substrate.

Fig. S6.

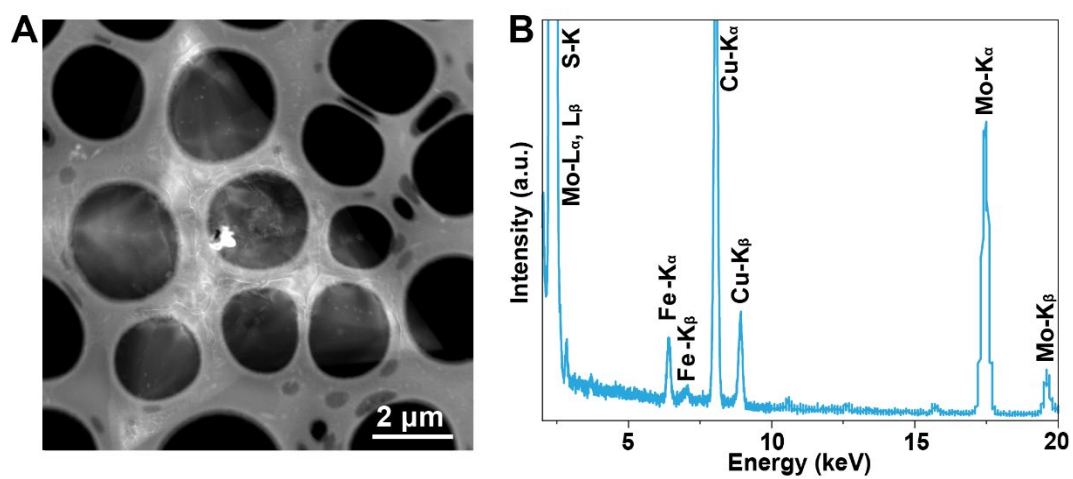


Fig. S6. (A) The HAADF-STEM image of a Fe-doped MoS₂ flake. (B) EDX spectrum of Fe-doped MoS₂ measured from sample in (A). The Cu signal comes from the TEM Cu grid.

Fig. S7.

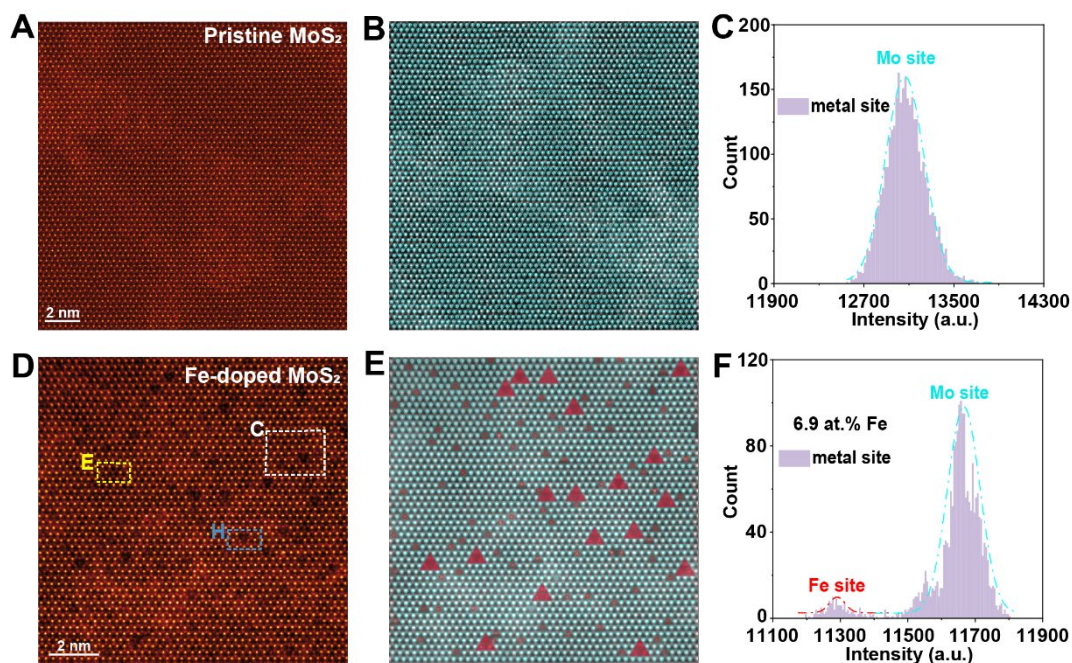


Fig. S7. Microscopic characterizations of monolayer pristine and Fe-doped MoS₂.

Atomic-scale HAADF-STEM images of monolayer (A) pristine and (D) Fe-doped MoS₂. The labelled sites of Mo atoms (cyan circles) and Fe atoms (red circles) for monolayer (B) pristine and (E) Fe-doped MoS₂. (C and F) The statistical charts of atomic intensity for labelled atoms in monolayer (B) pristine and (E) Fe-doped MoS₂. The white, yellow, and blue boxes in (D) are the interception positions of the enlarged atomic structure presented in Fig. 1 (C, E and H) in the main text, respectively. 3Fe_{Mo}-S associates in (E) are marked with red triangles, and it can be seen that Fe atoms substitute Mo atoms randomly.

Fig. S8.

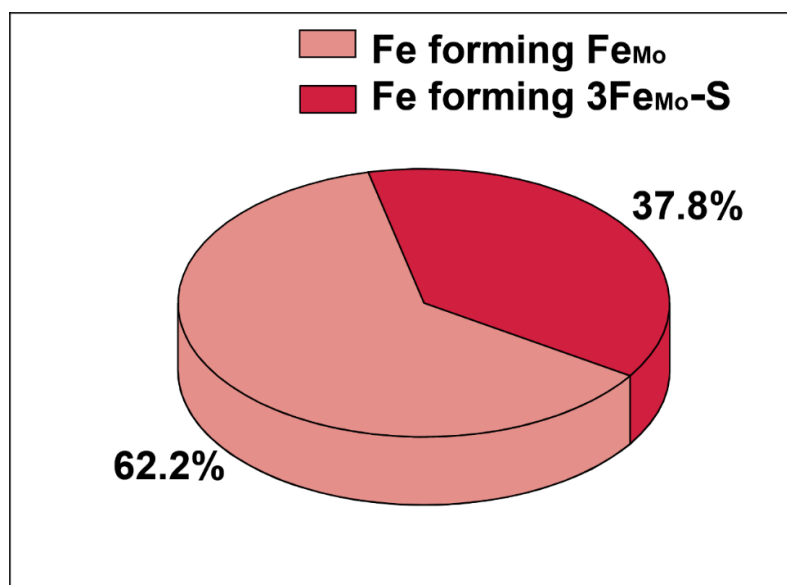


Fig. S8. The proportions of Fe atoms in different defect types in monolayer Fe-doped MoS₂ synthesized from Fe₂Mo₃O₁₂ precursor.

Fig. S9.

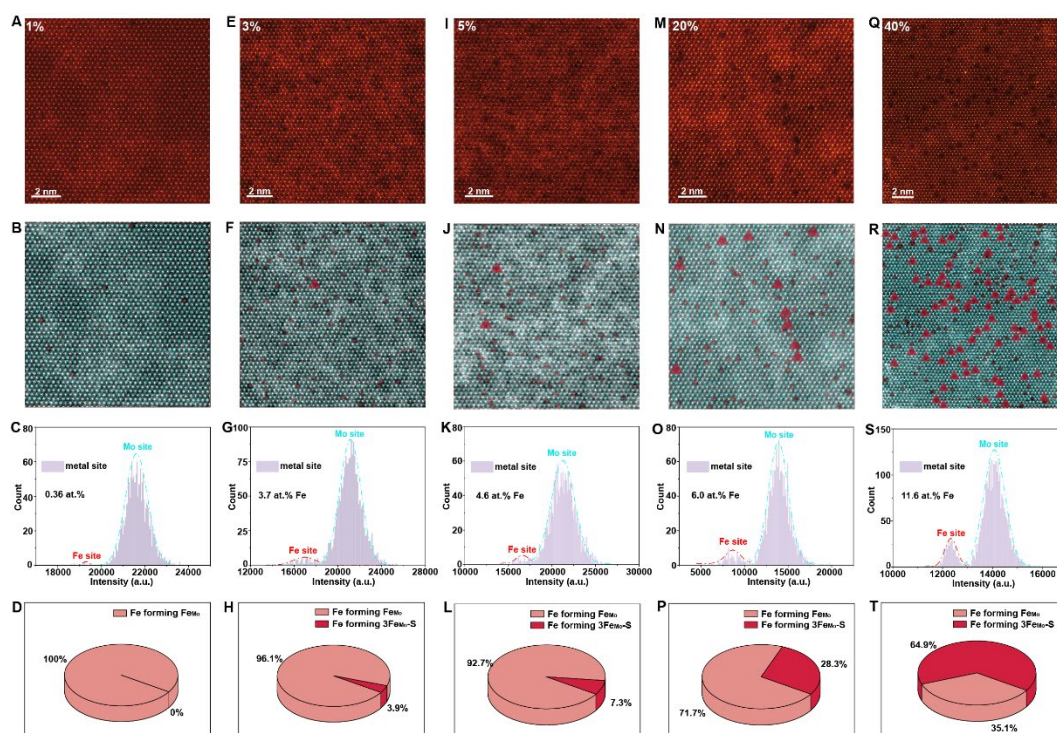


Fig. S9. Statistical analysis of Fe doping concentration in monolayer Fe-doped MoS₂ synthesized from FeS₂/MoO₃ mixture precursor with different mole ratios of Fe. Atomic HAADF-STEM images of monolayer Fe-doped MoS₂ grown with FeS₂ accounting for (A) 1 at. %, (E) 3 at. %, (I) 5 at. %, (M) 20 at. %, and (Q) 40 at. % in FeS₂-MoO₃ precursor. Metallic atom mapping of monolayer Fe-doped MoS₂ grown with FeS₂ accounting for (B) 1 at. %, (F) 3 at. %, (J) 5 at. %, (N) 20 at. %, and (R) 40 at. % in FeS₂-MoO₃ precursor, in which the positions of 3Fe_{Mo}-S associates are marked with red triangles. The cyan and red cycles are Mo sites and Fe sites, respectively. Statistical charts of atomic intensity for labelled atoms of monolayer Fe-doped MoS₂ grown with FeS₂ accounting for (C) 1 at. %, (G) 3 at. %, (K) 5 at. %, (O) 20 at. %, (S) 40 at. % in FeS₂-MoO₃ precursor and the proportions of Fe atoms in different defect types in monolayer Fe-doped MoS₂ grown with FeS₂ accounting for (D) 1 at. %, (H) 3 at. %, (L) 5 at. %, (P) 20 at. %, (T) 40 at. % in FeS₂-MoO₃ precursor. The red and pink areas in the pie chart represents the contents of 3Fe_{Mo}-S associate and isolated Fe_{Mo} point defect, respectively.

Fig. S10.

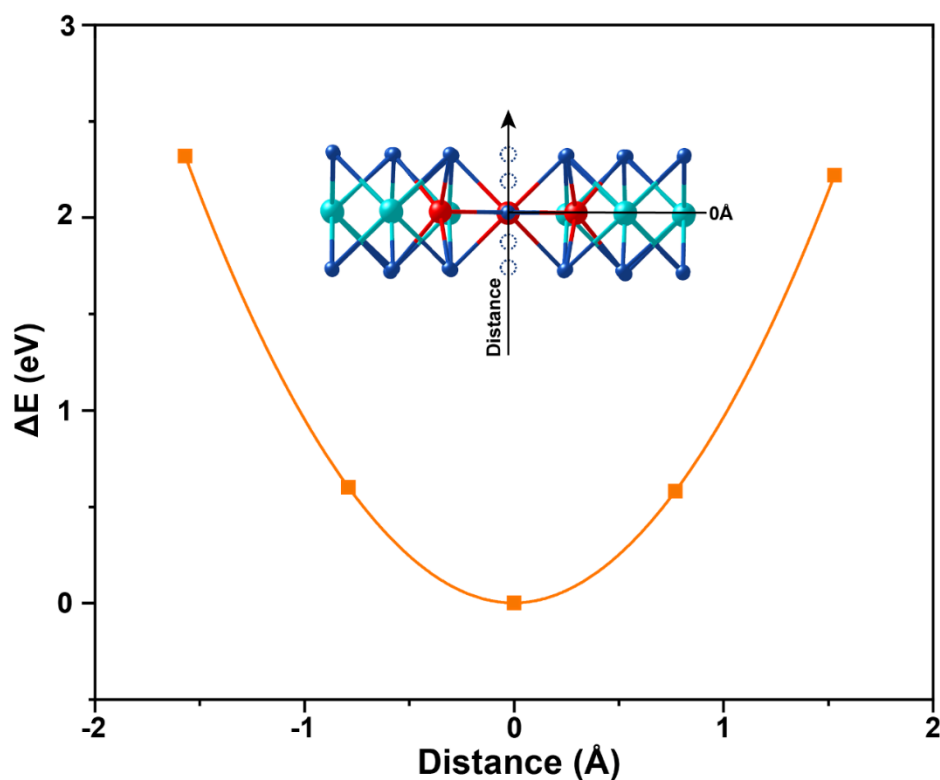


Fig. S10. The total energy difference (ΔE) of $3\text{Fe}_{\text{Mo}}\text{-S}$ associate with the position of the central S atom. Assuming that the plane of Fe atoms is the zero point of the coordinate axis, the moving distance of S atom is -1.57, -0.79, 0, 0.77 and 1.53 Å from the bottom to top. Set the ΔE of the system as 0 eV when the position of S atom is in the plane of Fe atoms, and the ΔE of the system from the bottom to top is 2.32, 0.6, 0, 0.58 and 2.22 eV, respectively.

Fig. S11.

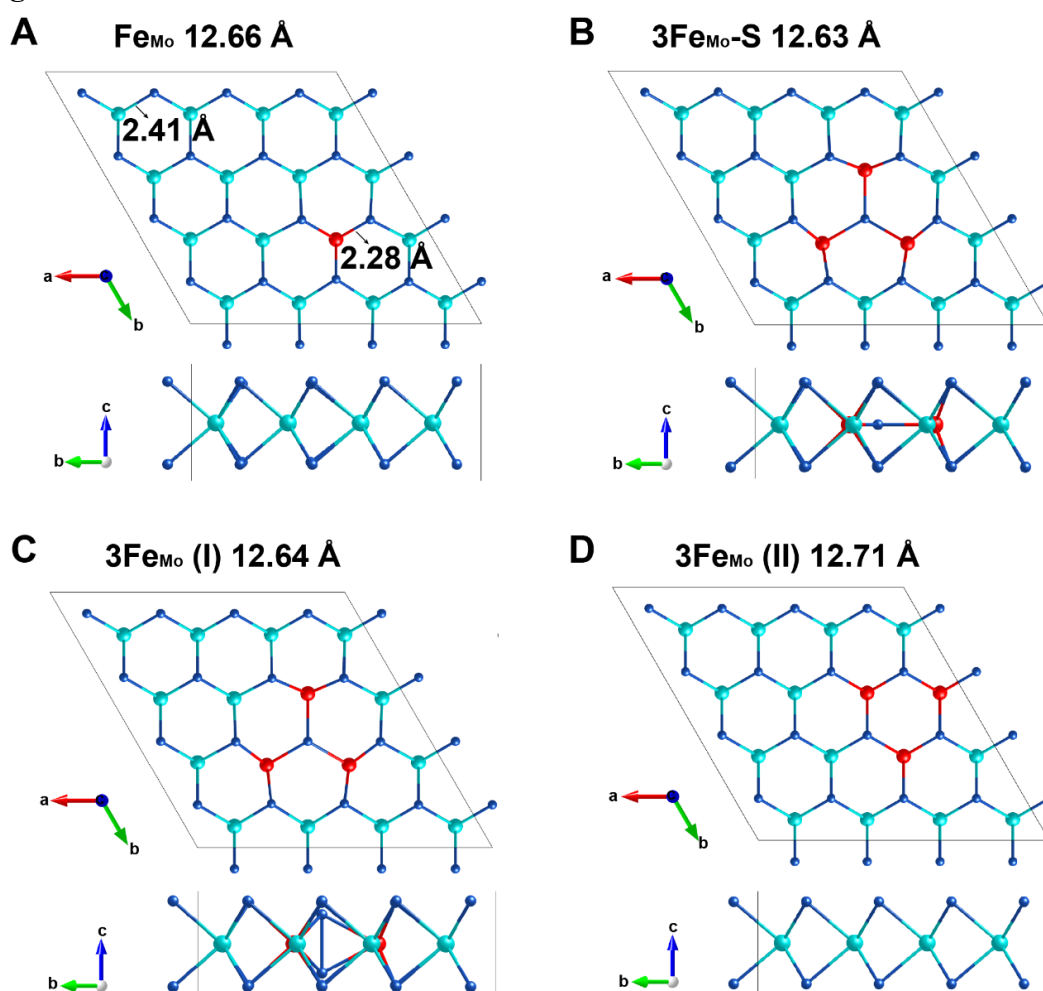


Fig. S11. The unit structures of $4\times 4\times 1$ supercell for monolayer Fe-doped MoS_2 with different Fe-containing configurations: (A) Fe_{Mo} , (B) $3\text{Fe}_{\text{Mo-S}}$, (C) 3Fe_{Mo} (I), (D) 3Fe_{Mo} (II). Plots display top (top panel) and side (bottom panel) views of these configurations. The corresponding chemical bond length is indicated by arrows in (A). The lattice parameters of every configuration after relaxation are also outlined. Blue, cyan, and red spheres denote S, Mo, and Fe atoms, respectively. The length marked in every figure is the cell parameter (side length of diamond border) of each $4\times 4\times 1$ supercell.

Fig. S12.

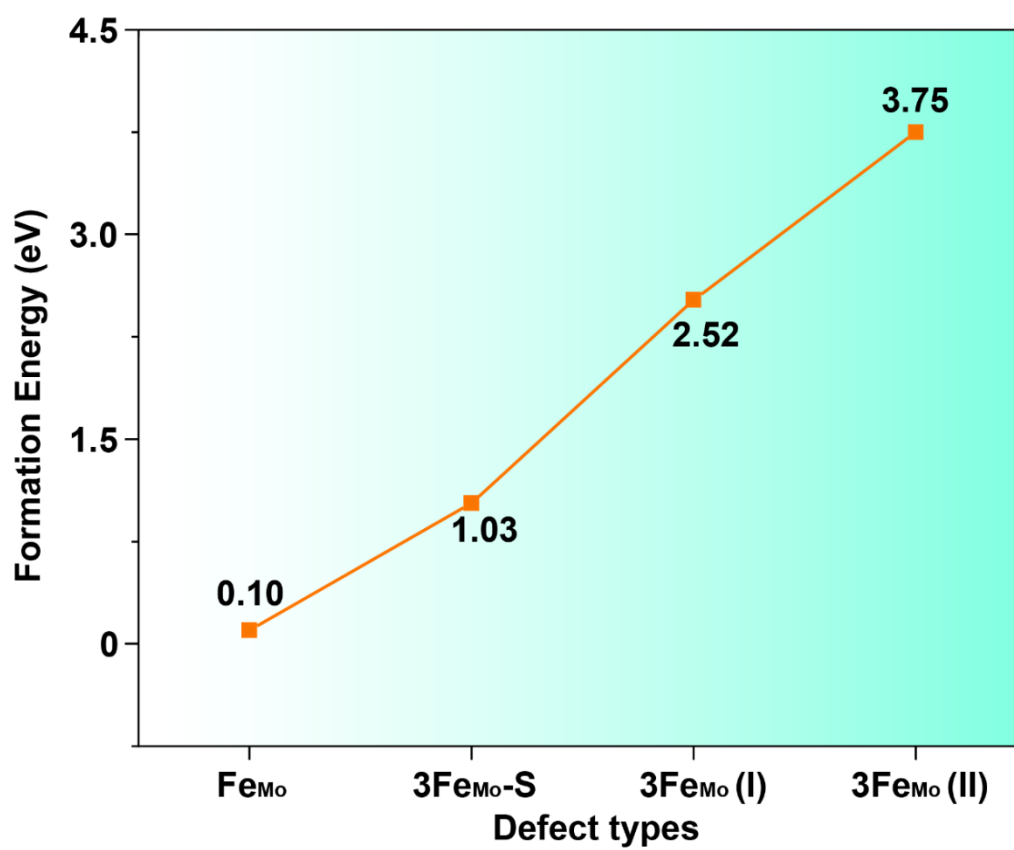


Fig. S12. The formation energy of FeMo point defect, 3FeMo-S associate, 3FeMo (I) and 3FeMo (II) under S-rich condition.

Fig. S13.

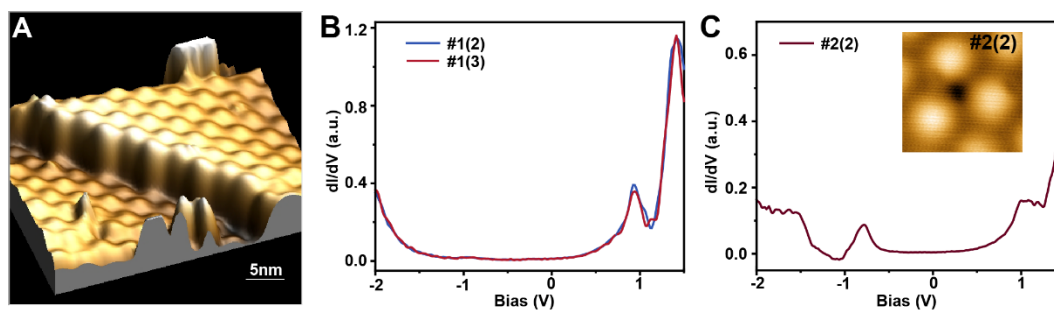


Fig. S13. (A) Corresponding 3D image of the atomic structure shown in Fig. 2A in the main text. dI/dV spectra in the center of (B) defect #1(2) and defect #1(3) as marked in Fig. 2A in the main text. (C) dI/dV spectrum in the center of defect #2(2) located at another position (inset).

Fig. S14.

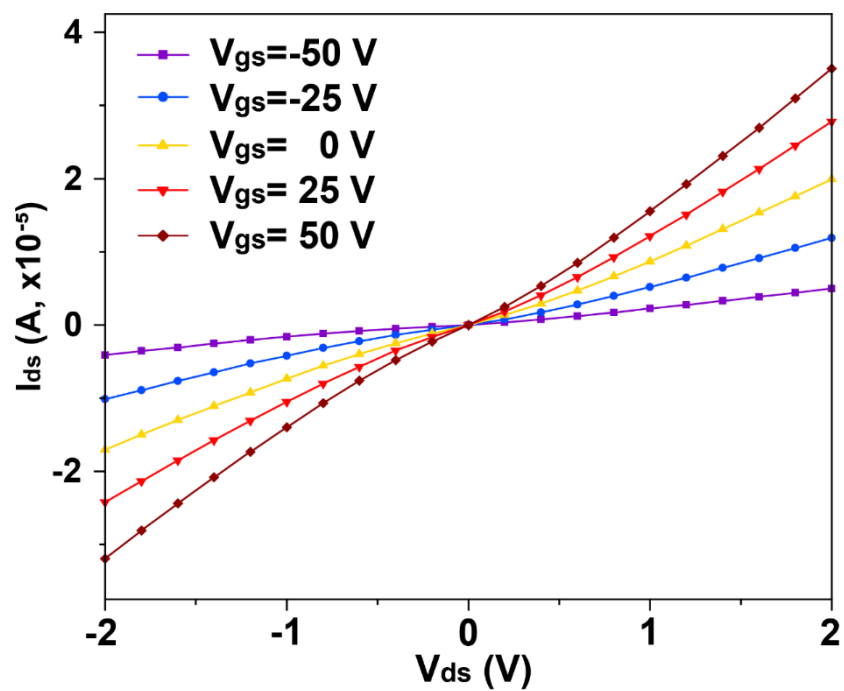


Fig. S14. The output curves of monolayer pristine MoS₂.

Fig. S15.

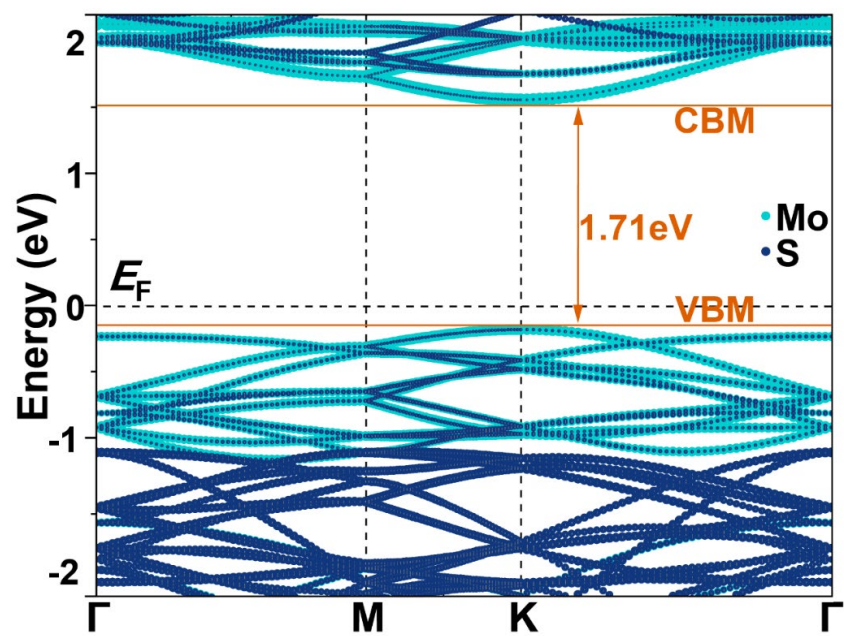


Fig. S15. The calculated band structure of monolayer pristine MoS₂. The cyan and dark blue dots represent the contribution of Mo and S atoms, respectively.

Fig. S16.

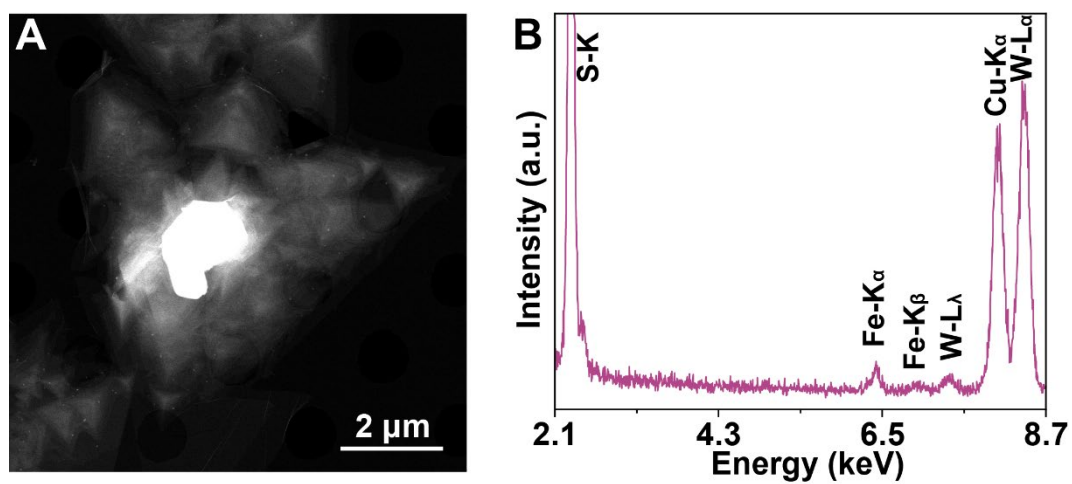


Fig. S16. (A) The HAADF-STEM image of a Fe-doped WS₂ flake. (B) EDX spectrum of Fe-doped MoS₂ measured from sample in (A).

Fig. S17.

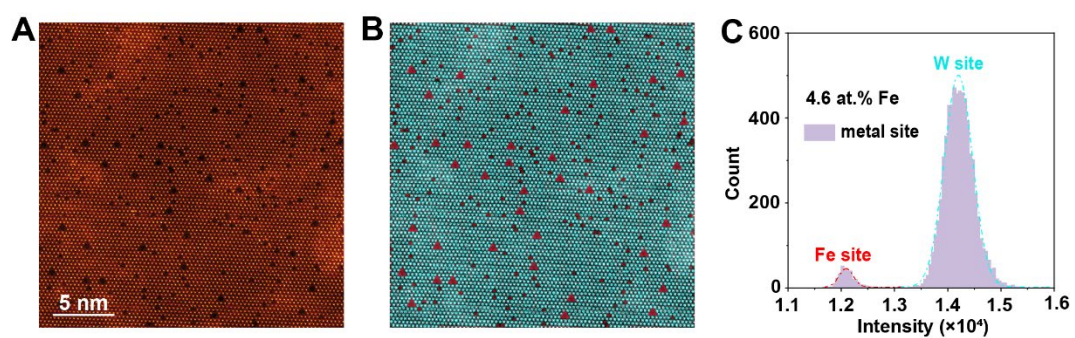


Fig. S17. Microscopic characterizations of monolayer Fe-doped WS₂. (A) Atomic-scale HAADF-STEM images of monolayer Fe-doped WS₂. (B) The labelled sites of W atoms (cyan circles) and Fe atoms (red circles) for monolayer Fe-doped WS₂. (C) The statistical charts of atomic intensity for labelled atoms in monolayer Fe-doped WS₂.

Table S1.

Table S1. Calculated Raman vibrational modes of monolayer pristine MoS₂. Phonon frequencies and irreducible representations of monolayer MoS₂ at Γ , M, and K high-symmetry points from our DFT calculations. Groups of the wave vector are also labeled.

$\Gamma(D_{3h})$	$\omega(cm^{-1})$	$M(C_{2v})$	$\omega(cm^{-1})$	$K(C_{3h})$	$\omega(cm^{-1})$
$A_2''(ZO)$	453.8	A_1	390.7	A'	387.9
$A_1'(ZO)$	391.6	B_1	368.2	E''	360.7
$E'(LO)$	366.0	B_2	349.3	E'	352.8
$E'(TO)$	366.0	A_1	340.1	E'	316.0